nature energy

Article

https://doi.org/10.1038/s41560-023-01310-y

Phase-heterojunction all-inorganic perovskite solar cells surpassing 21.5% efficiency

In the format provided by the authors and unedited

Table of contents

Captions for **Supplementary Video 1**: In-situ deposition of γ–$CsPbI_3$-GAI based perovskite thin film by thermal evaporation at module scale (13 cm x 13 cm= 169 cm^2).

Captions for **Supplementary Video 2**: Testing of 13 x 13 cm^2 PHS-based module under LED lamp in ambient conditions.

Other Supplementary Materials for this manuscript include the following:

Supplementary Movies 1
Supplementary Movies 2

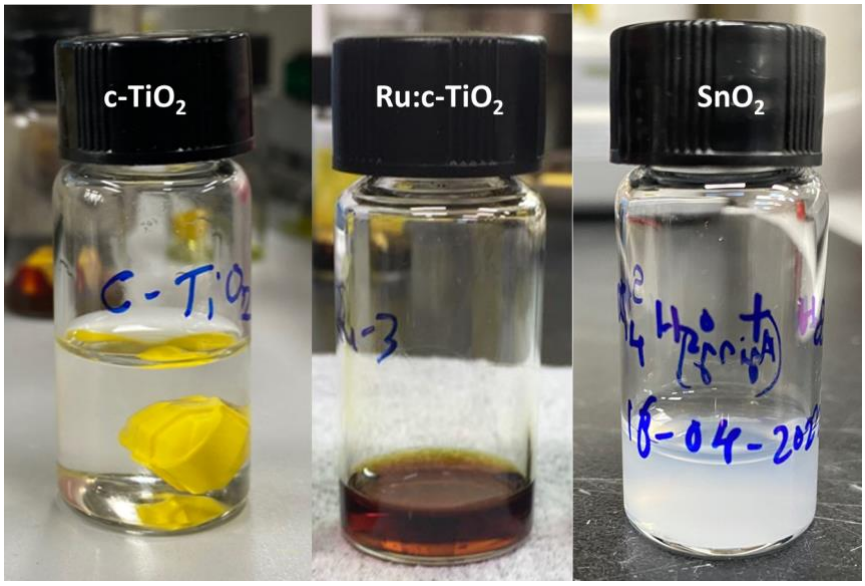

Supplementary Figure 1| Preparation of modified ETL. Photographs of c-TiO_2, Ru:c-TiO_2, and SnO_2 colloidal solution aged (one week)**.**

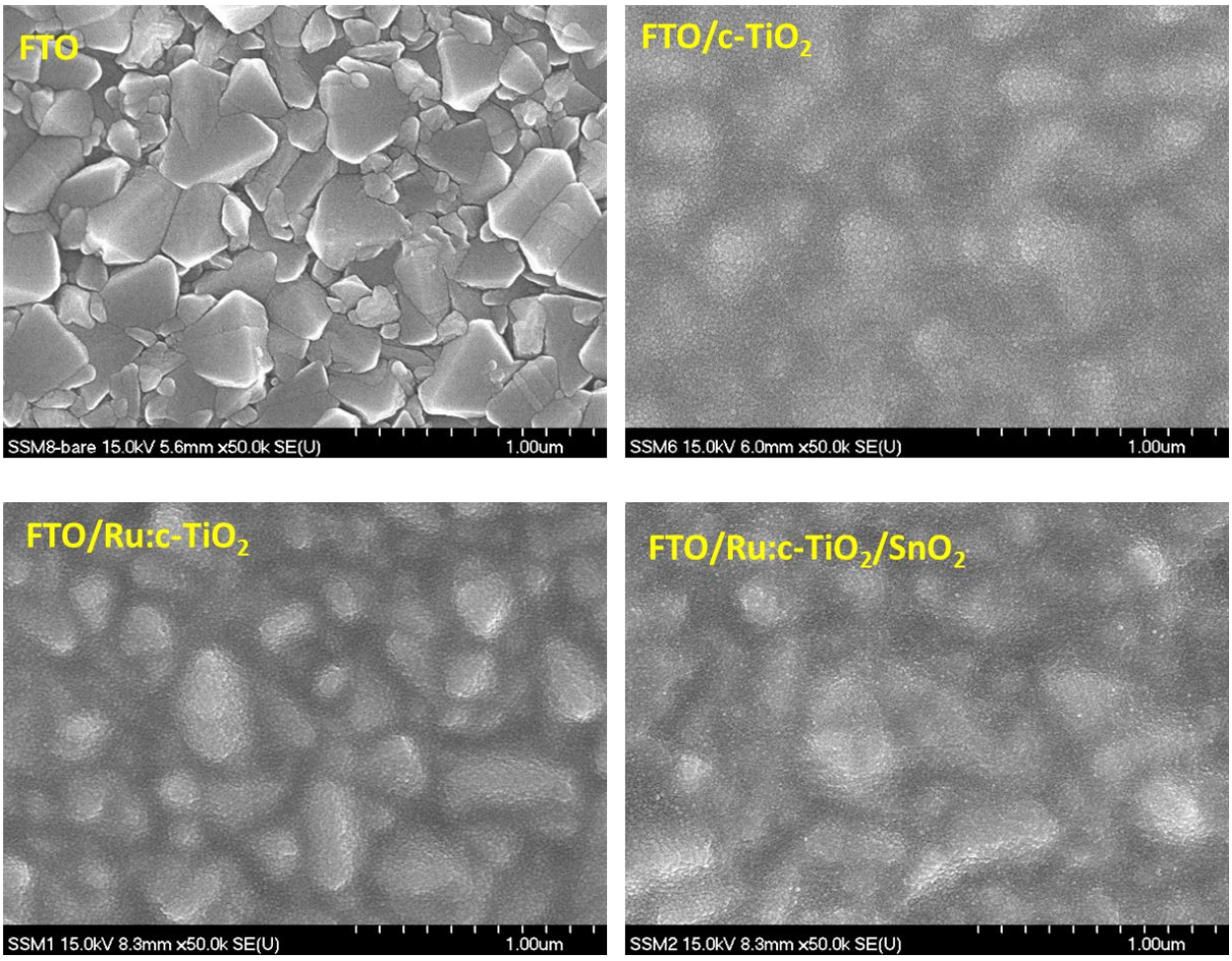

Supplementary Figure 2| SEM images of different ETLs deposited on FTO substrates.

Supplementary Table 1. Detailed thermal evaporation parameters for individual materials.* *We observed various deposition rates for PEAI and GAI for this current. We recommend carefully tuning the current between this range results in good composition.*

Precursor	**PbI_2**	**CsI**	**GAI**
Set rate (Å/s)	0.7-0.8	0.65-0.75	0.05-0.1
Temperature (^oC)	310-330	445-455	145-150
Current required (Amp)	45-50	65-70	35-40*
Heating source	Q-Crucible		

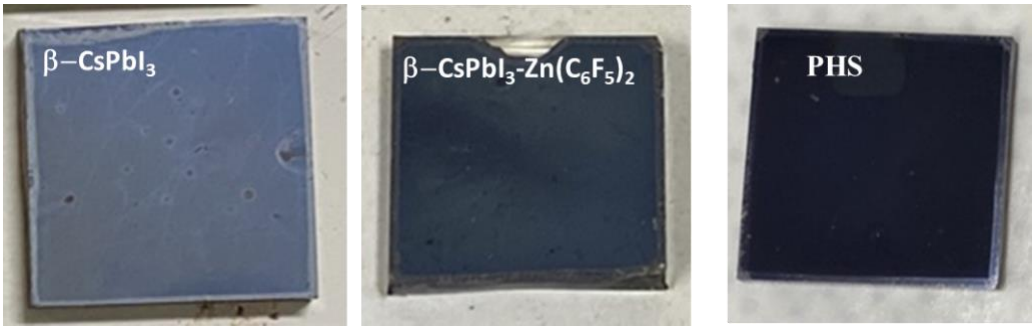

Supplementary Figure 3| Stability of β–$CsPbI_3$, β–$CsPbI_3$-$Zn(C_6F_5)_2$ and γ–$CsPbI_3$-GAI (90 nm), on to β–$CsPbI_3$-$Zn(C_6F_5)_2$ thin film and stored in ambient condition over 24 hours. Relative humidity 25-30 %.

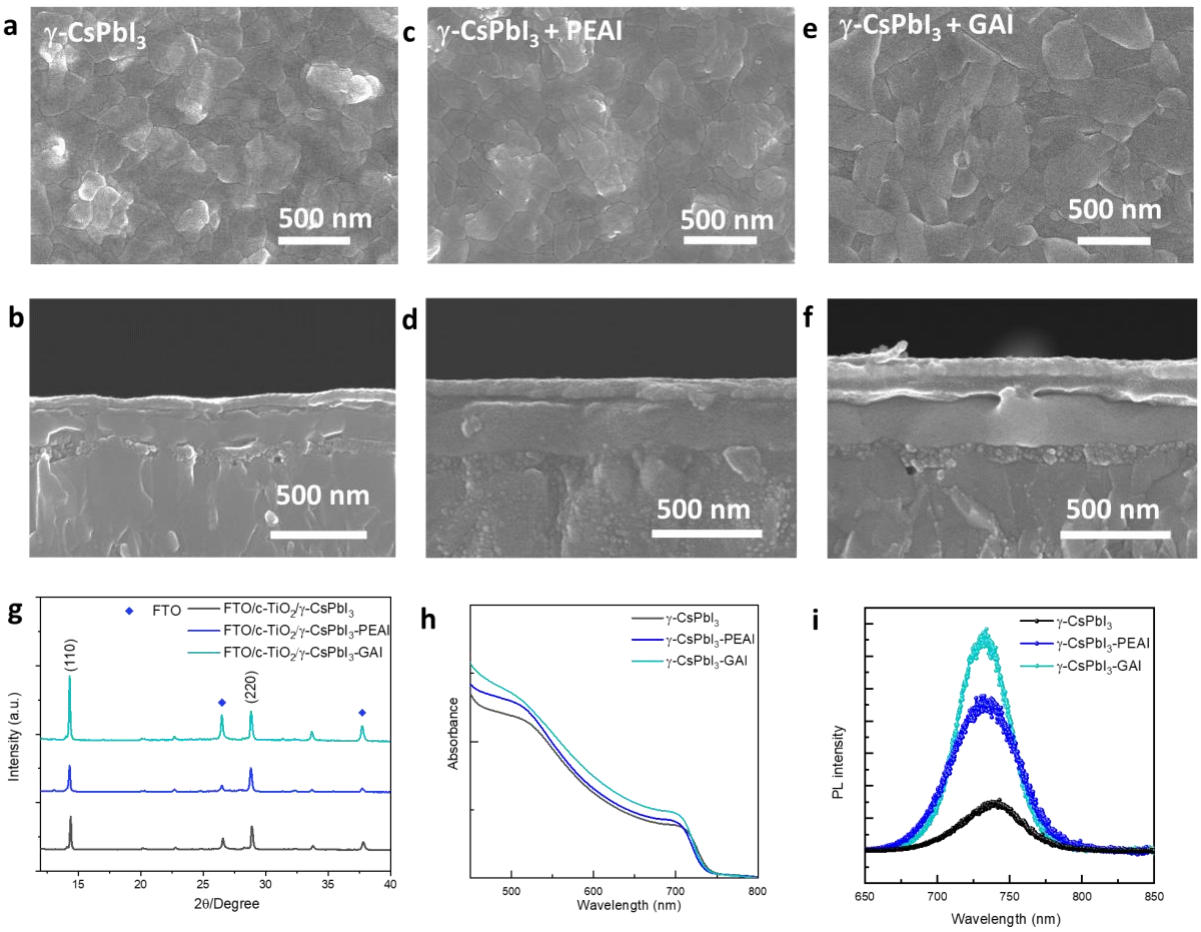

Supplementary Figure 4|All thermally evaporated γ-CsPbI3 thin films. Top and cross-sectional SEM images of the γ-CsPbI3 perovskite thin films and complete device deposited by triple source thermal evaporation. (**a** and **b**) control. (**c** and **d**) PEAI assisted. (**e** and **f**) GAI assisted γ-CsPbI3 perovskite thin film. **g**. XRD patterns of γ-CsPbI3, γ-CsPbI3-PEAI and γ-CsPbI3-GAI deposited on FTO-c-TiO2 substrate. **h.** UV-vis optical absorption spectra and **i.** PL spectra.

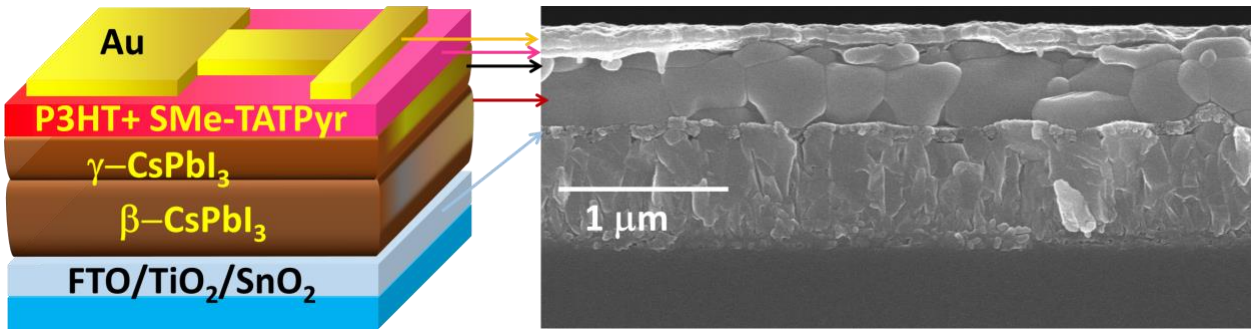

Supplementary Figure 5| Schematic representation of PHS device and respective cross-sectional SEM image.

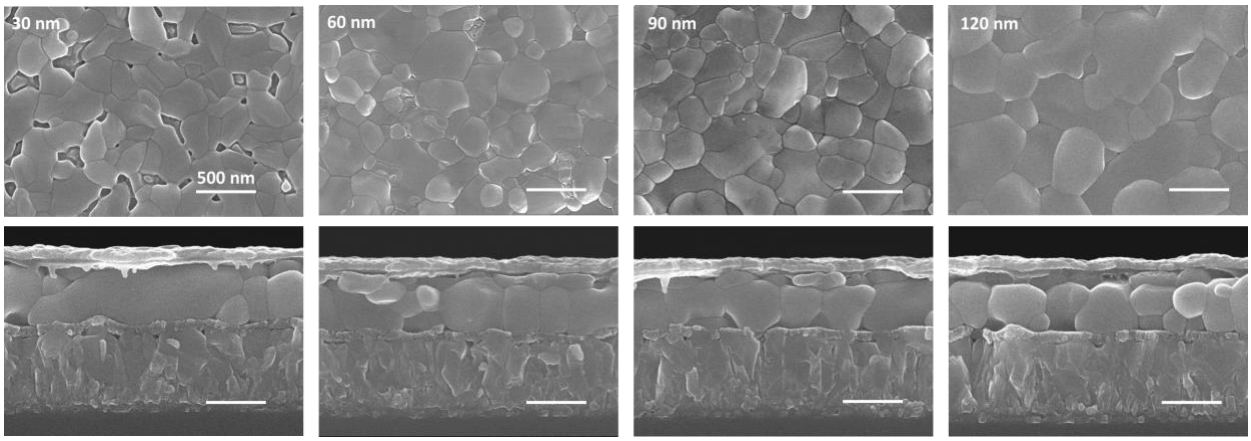

Supplementary Figure 6| Thermally evaporated γ–$CsPbI_3$ thin films. Top and cross-sectional SEM images of the γ–$CsPbI_3$-GAI perovskite thin film and device deposited by thermal evaporation with different top layer thicknesses. All scale bars are 500 nm. Inset values show the rear γ–$CsPbI_3$-GAI film thickness.

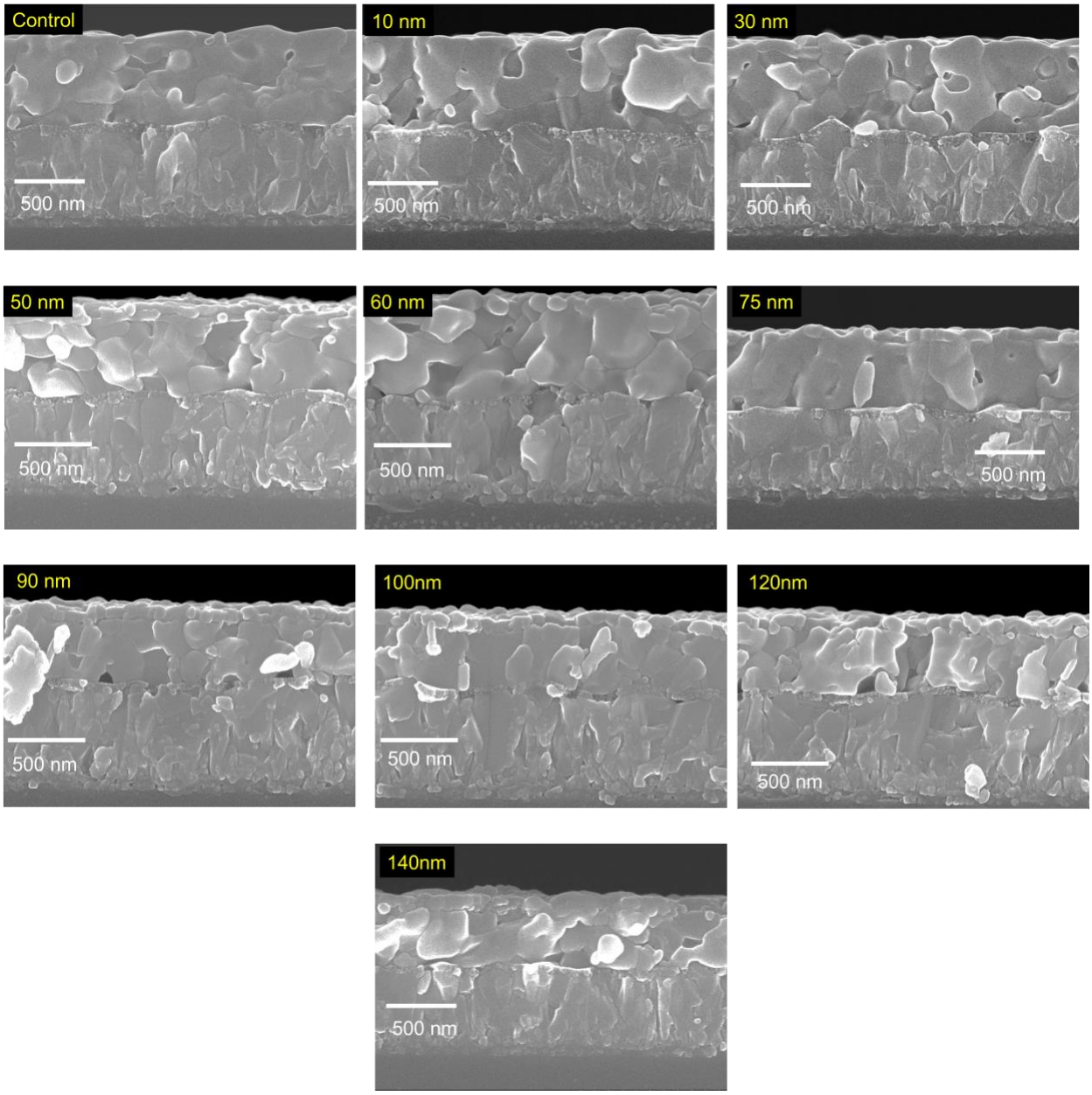

Supplementary Figure 7| Cross-sectional SEM images of β-$CsPbI_3$-$Zn(C_6F_5)_2$ thin films with different thicknesses of γ-$CsPbI_3$-GAI rear absorber.

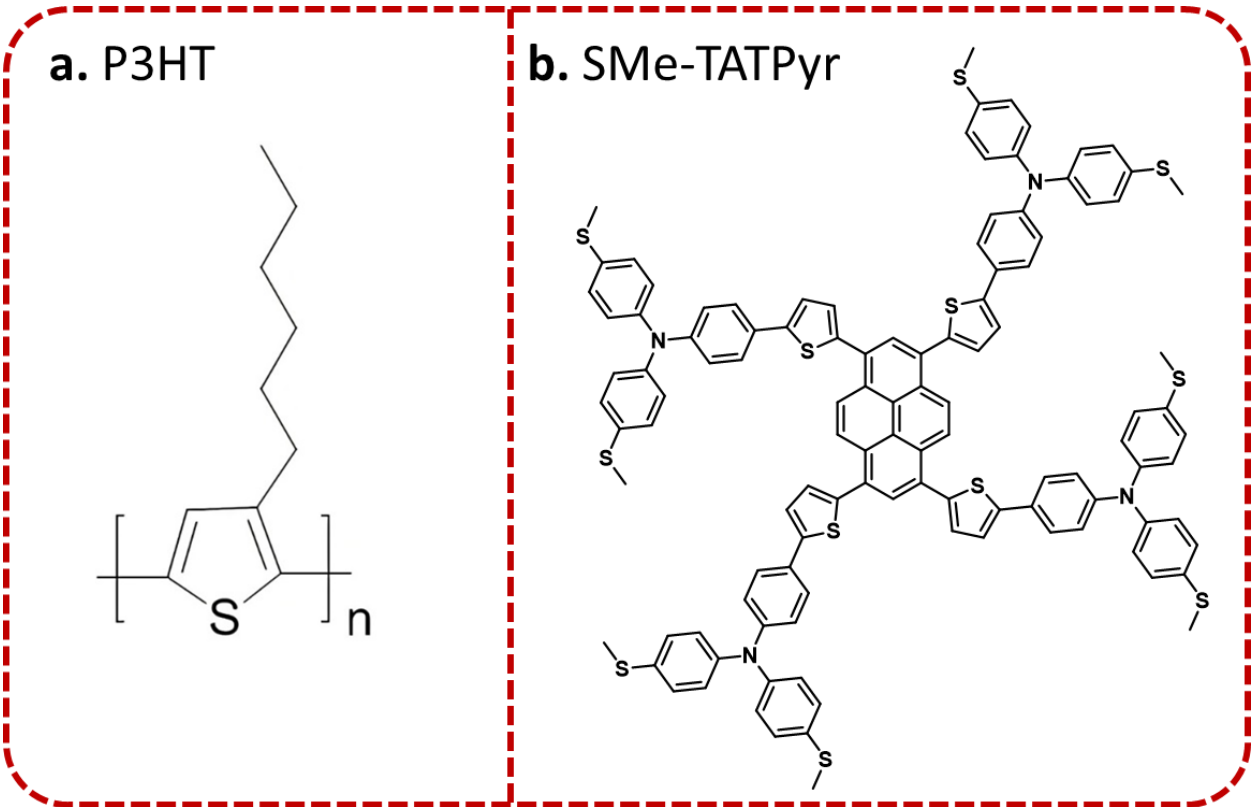

Supplementary Figure 8| Chemical structures of **a**. P3HT and **b**. SMe-TATPyr HTL was used in the present study.

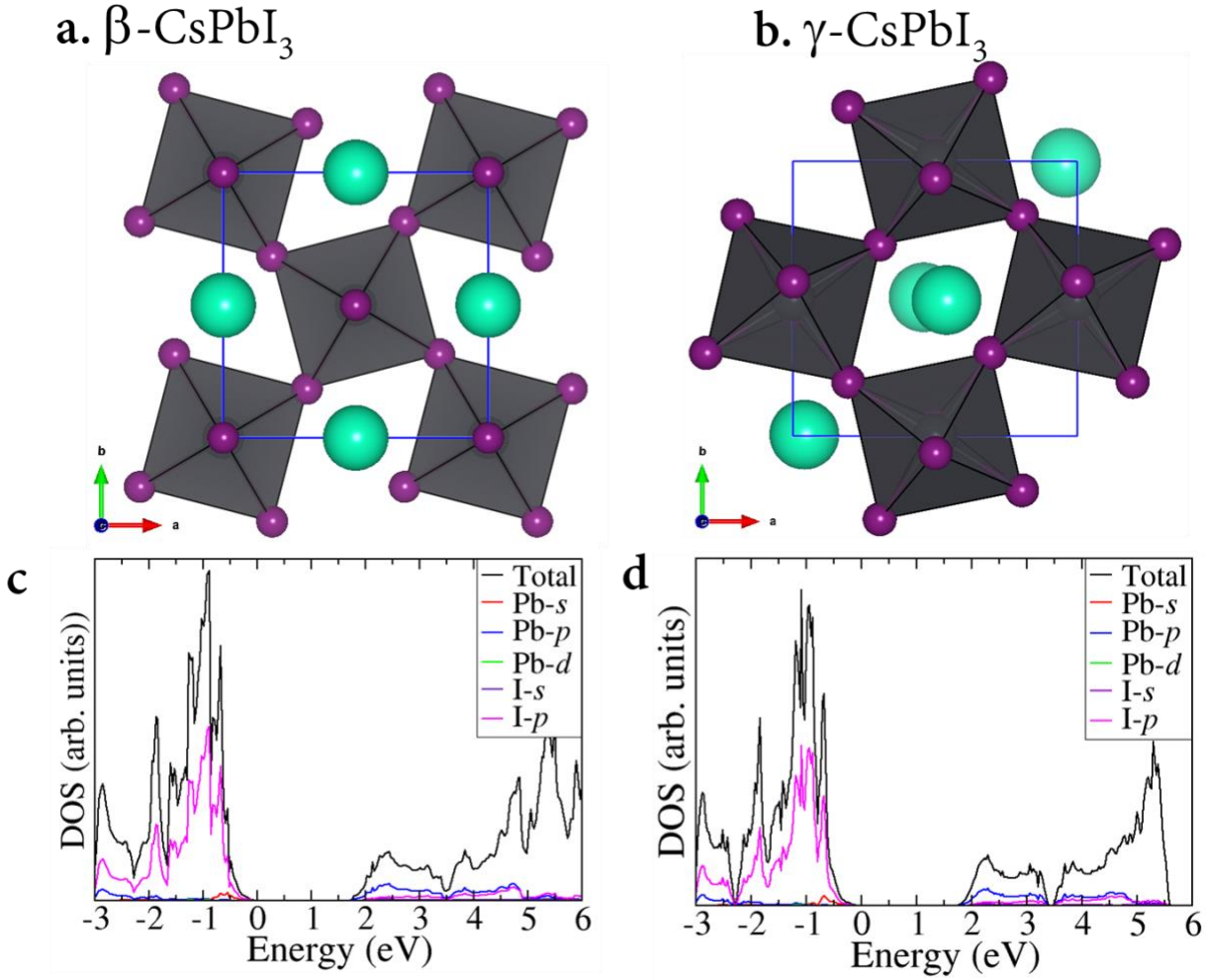

Supplementary Figure 9| Crystal structure and partial density of state of $CsPbI_3$. Crystal structures of (a) tetragonal β-$CsPbI_3$ and (b) orthorhombic γ-$CsPbI_3$. The corresponding partial density of state are shown in (c) and (d), respectively.

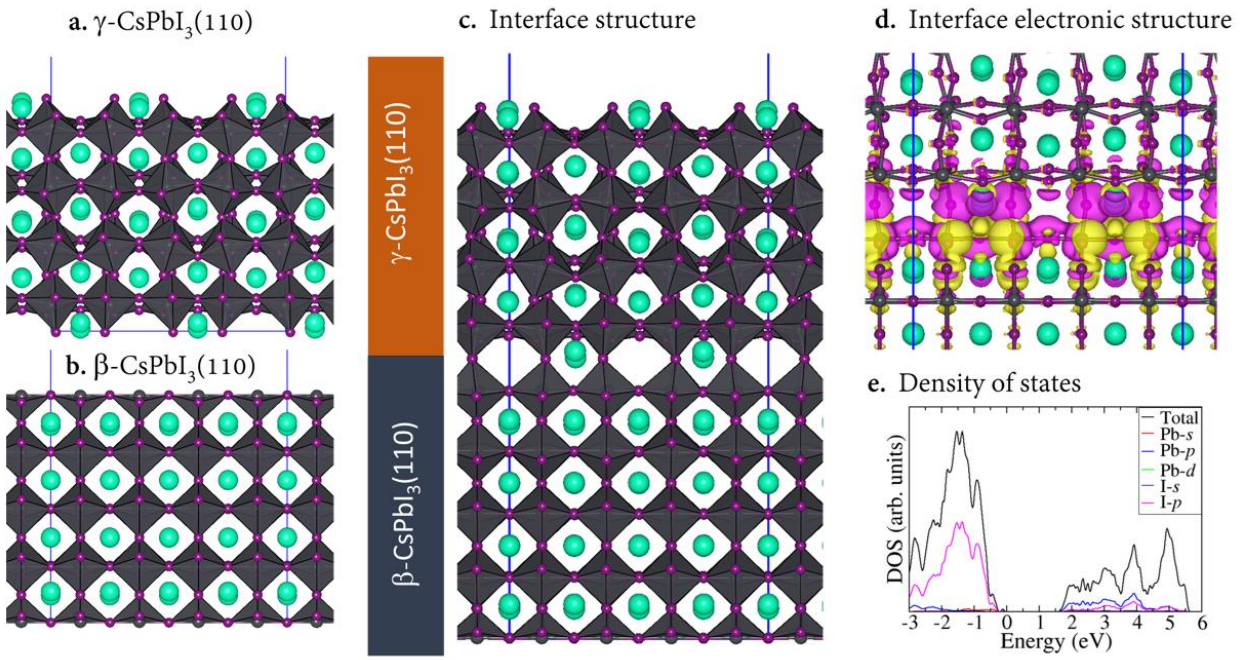

Supplementary Figure 10| Geometry optimized structures of the isolated $CsPbI_3$. a. γ-$CsPbI_3$ (110) and **b.** β-$CsPbI_3$(110) surfaces used for the phase heterojunction construction. **c.** Illustration of the developed 3 × 3 × 3 supercell crystal structures at the β–$CsPbI_3$ (110) /γ–$CsPbI_3$ (110) interface. **d.** The differential charge density isosurfaces for the β-$CsPbI_3$/γ-$CsPbI_3$ phase junction with an iso-value of 0.01 e $Å^{-3}$ (purple and yellow regions represent the charge depletion and accumulation in the space, respectively). **e.** The electronic density of states of the β-$CsPbI_3$/γ-$CsPbI_3$ phase junction showing no gap states.

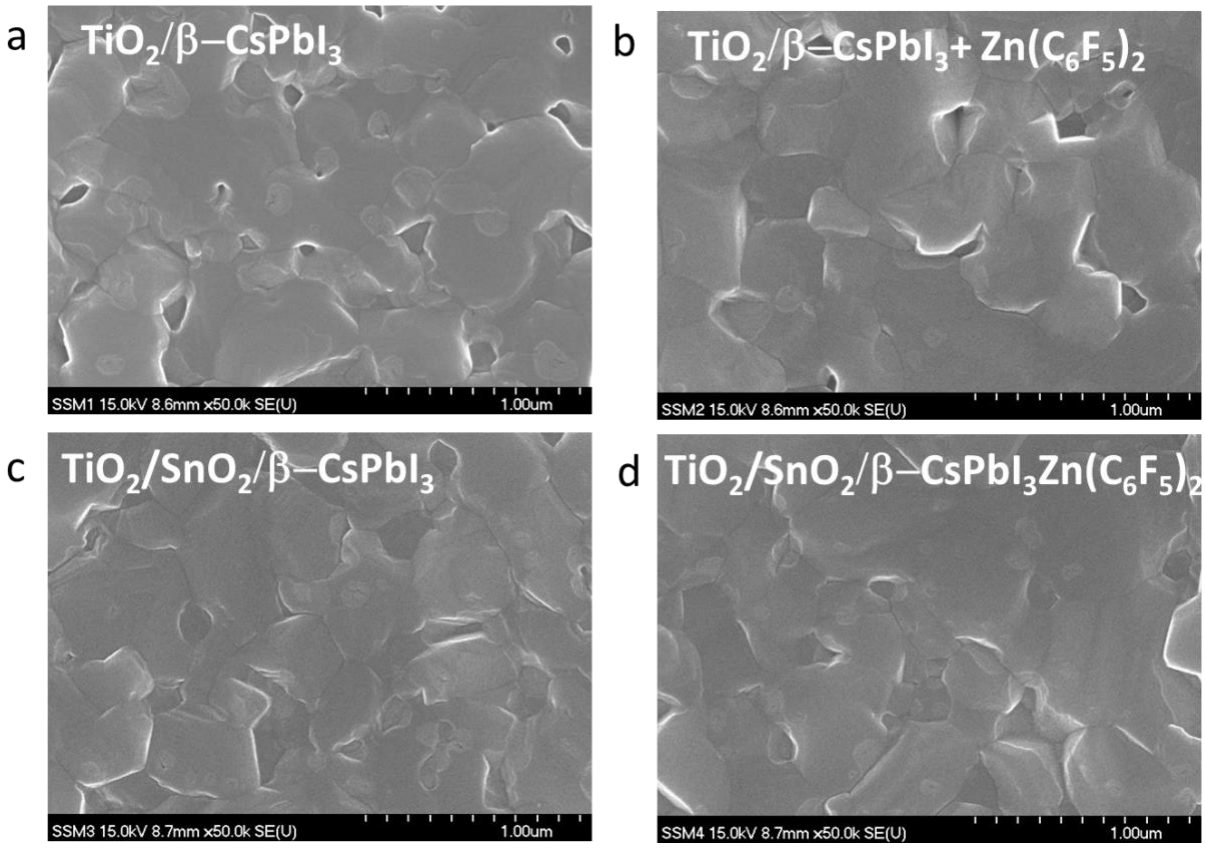

Supplementary Figure 11 | Influence of different ETLs on the surface morphology of the β-$CsPbI_3$ thin films deposited in ambient conditions using the hot-air method. a.β-$CsPbI_3$ thin film deposited by hot-air method on Ru:c-TiO_2, **b.** β-$CsPbI_{3+}$ $Zn(C_6F_5)_2$ thin film deposited by hot-air method on Ru:c-TiO_2, **c** and **d.** β-$CsPbI_{3+}$ $Zn(C_6F_5)_2$ and β-$CsPbI_{3+}$ $Zn(C_6F_5)_2$ thin films deposited on Ru:c-TiO_2/SnO_2 ETLs.

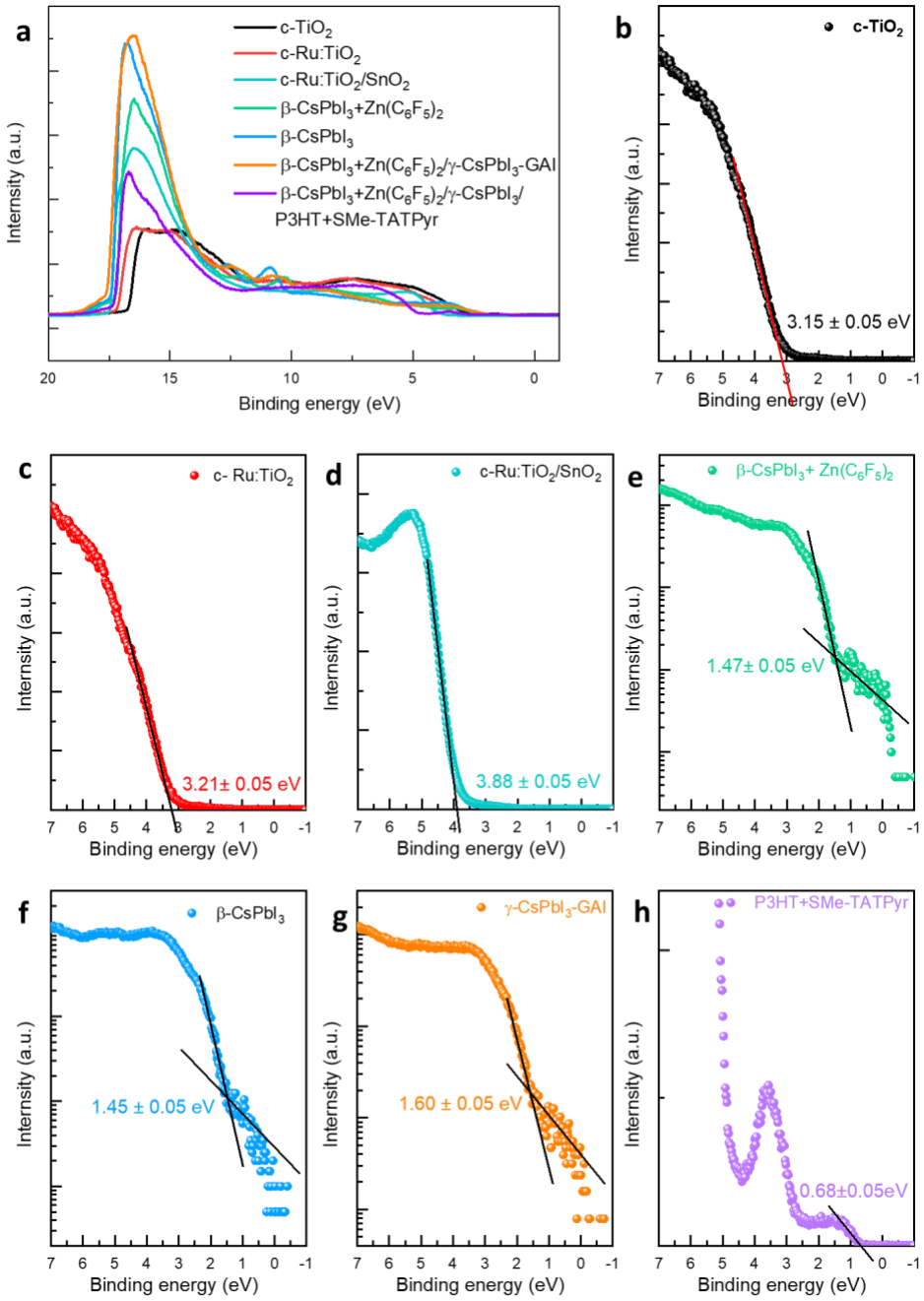

Supplementary Figure 12| Ultra-violet photoelectron spectroscopy (UPS). **a**. UPS survey spectra and **b-h**. valence band region of the different ETLs, $CsPbI_3$ perovskite thin films deposited by different methods and HTL. The fitting lines (VBM values) in b-h are obtained by fitting plots guides to the eye.

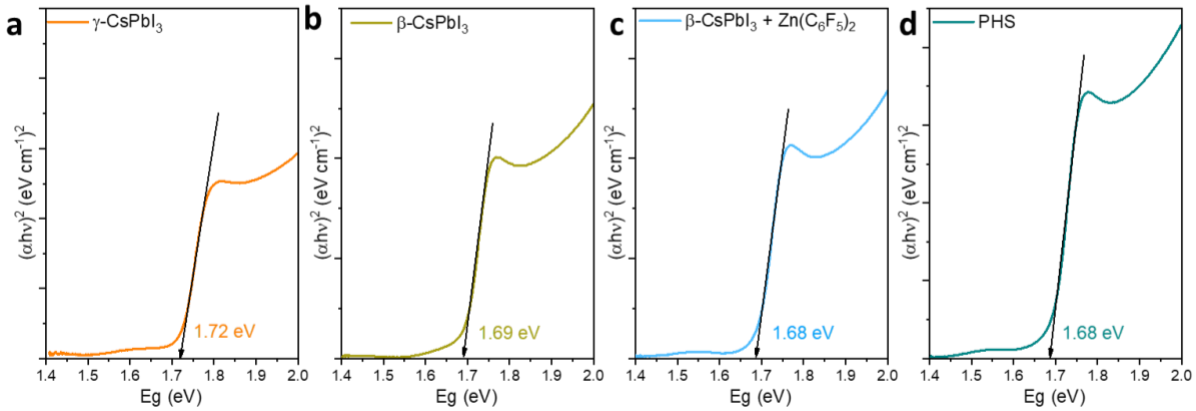

Supplementary Figure 13| Tauc plots of $CsPbI_3$ thin films. (**a-d**) Tauc plots for γ-$CsPbI_3$, β-$CsPbI_3$, β-$CsPbI_3$ + $Zn(C_6F_5)_2$ and PHS-based thin films. Plots were calculated from absorption data for **Fig. 3b**. The fitting lines in a-d are obtained by a linear fitting of data points.

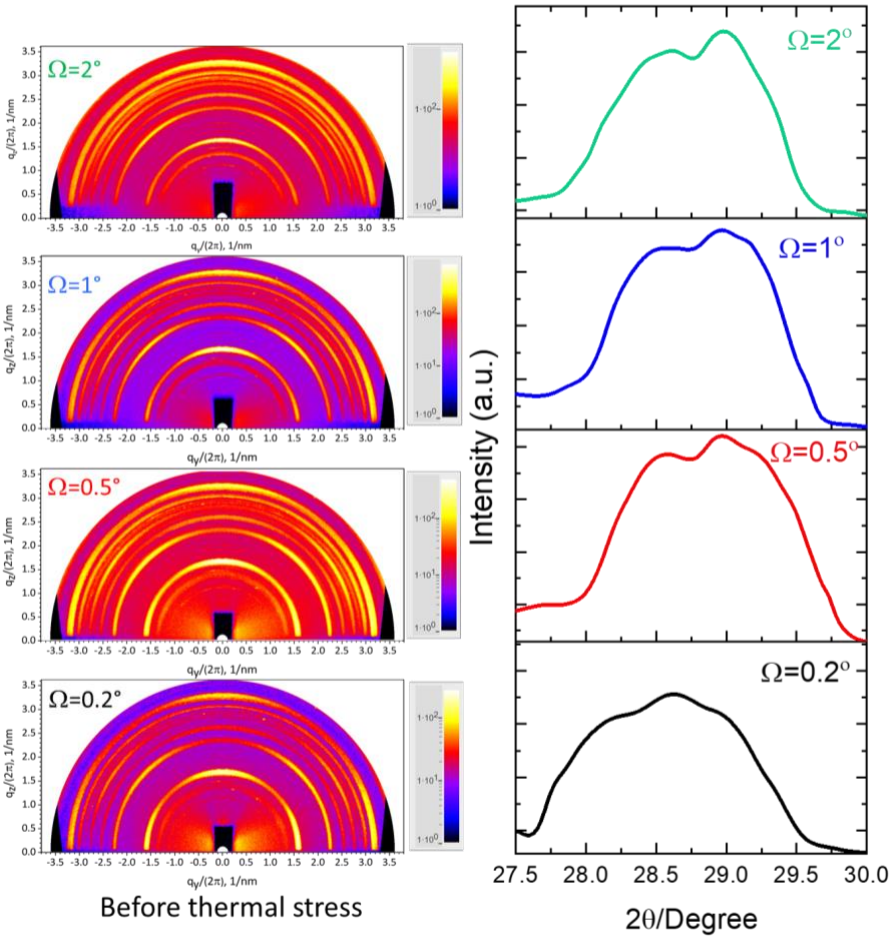

Supplementary Figure 14| Phase-stability of PHS absorbers on a single substrate before thermal stress. GIWAX images of the β-$CsPbI_3$-$Zn(C_6F_5)_2$/γ-$CsPbI_3$-GAI PHS thin film (left panel) and GIXRD analysis of PHS thin film measured at different incidence angles (**Ω**=0.2, 0.5, 1 and 2 °) before thermal stress. The respective left panel shows 2D GIWAX images and the right panel shows magnified XRD patterns from 27.5 to 30 °.

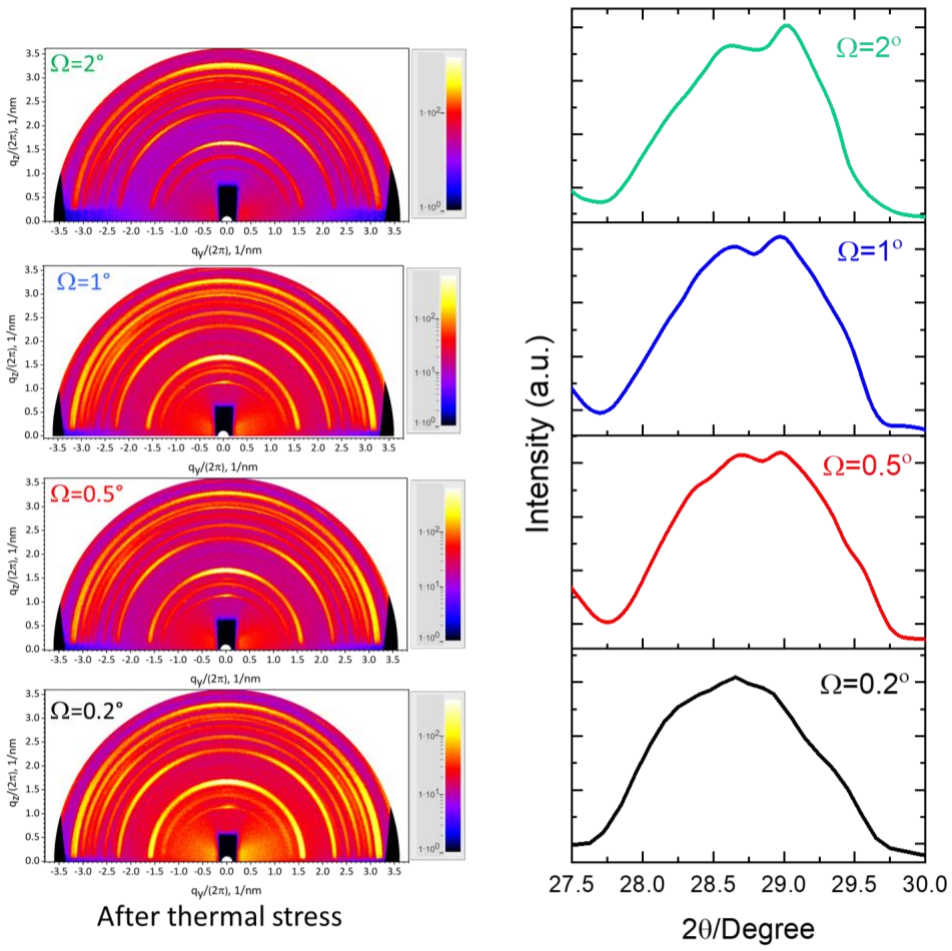

Supplementary Figure 15| Thermal stability of PHS absorbers on a single substrate after thermal stress. GIWAX images of the β-$CsPbI_3$-$Zn(C_6F_5)_2$/γ-$CsPbI_3$-GAI PHS thin film (left panel) and GIXRD analysis of PHS thin film measured at different incidence angles (**Ω**=0.2, 0.5, 1 and 2 °) after 85 °C thermal stress (1 hour). The respective left panel shows 2D GIWAX images and the right panel shows magnified XRD patterns from 27.5 to 30 °.

Supplementary Table 2. Summary of the band structure and energy levels for c-TiO_2, c-Ru:TiO_2, SnO_2, β-$CsPbI_3$+$Zn(C_6F_5)_2$, β-$CsPbI_3$, γ-$CsPbI_3$ and P3HT+SMe-TATPyr thin films.

Sample	E_{cutoff} (eV) (±0.05)	WF (ϕ) (eV)	VBM-E_F (eV) (±0.05)	VBM (eV)	ΔE_g (eV)	CBM (eV)
c-TiO_2	17.00	4.22	3.15	7.37	3.30	4.07
Ru:c-TiO_2	17.17	4.05	3.21	7.26	3.25	4.01
Ru:c-TiO_2/SnO_{2_R}	17.45	3.77	3.88	7.65	3.75	3.90
β-$CsPbI_3$+ $Zn(C_6F_5)_3$	17.24	3.98	1.47	5.45	1.68	3.77
β-$CsPbI_3$	17.37	3.85	1.45	5.32	1.69	3.63
γ-$CsPbI_3$-GAI	17.60	3.62	1.60	5.22	1.72	3.50
P3HT+SMe-TATPyr	17.33	3.89	0.68	4.57	1.92	2.65

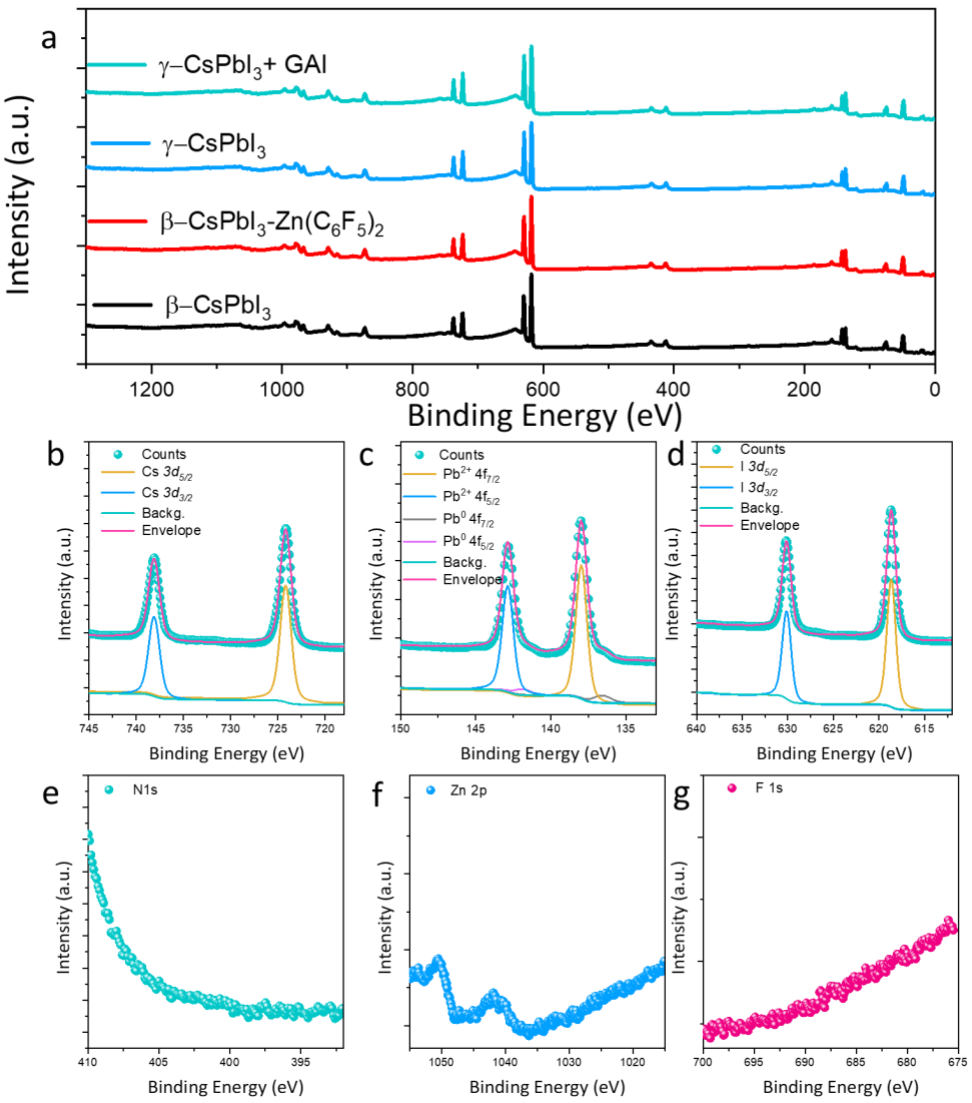

Supplementary Figure 16| a. XPS survey spectra of β–$CsPbI_3$, β–$CsPbI_3$-$Zn(C_6F_5)_2$, γ–$CsPbI_3$ and γ–$CsPbI_3$-GAAI based perovskite thin films. **b-g.** XPS fittings for the Cs 3d, Pb 4f, I 3d, N 1s, Zn 2p and F 1s core levels for the controlled β–$CsPbI_3$ sample. The counts and envelope (fit) have been offset to make the fittings clearer. Full details of peak positions can be found in **Supplementary Table 3**.

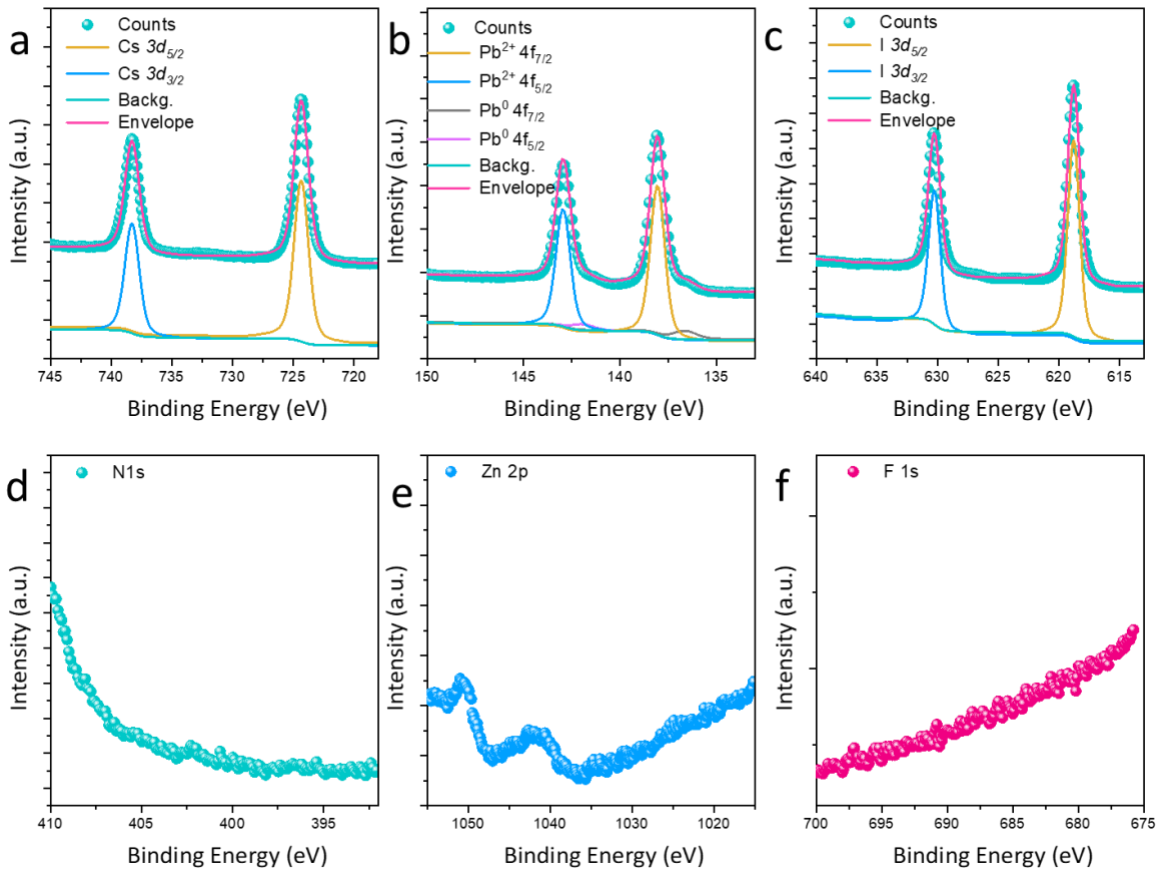

Supplementary Figure 17| a-f. XPS fittings for the Cs 3d, Pb 4f, I 3d, N 1s, Zn 2p and F 1s core levels for the controlled β–$CsPbI_3$-$Zn(C_6F_5)_2$ sample. The counts and envelope (fit) have been offset to make the fittings clearer. Full details of peak positions can be found in **Supplementary Table 3**.

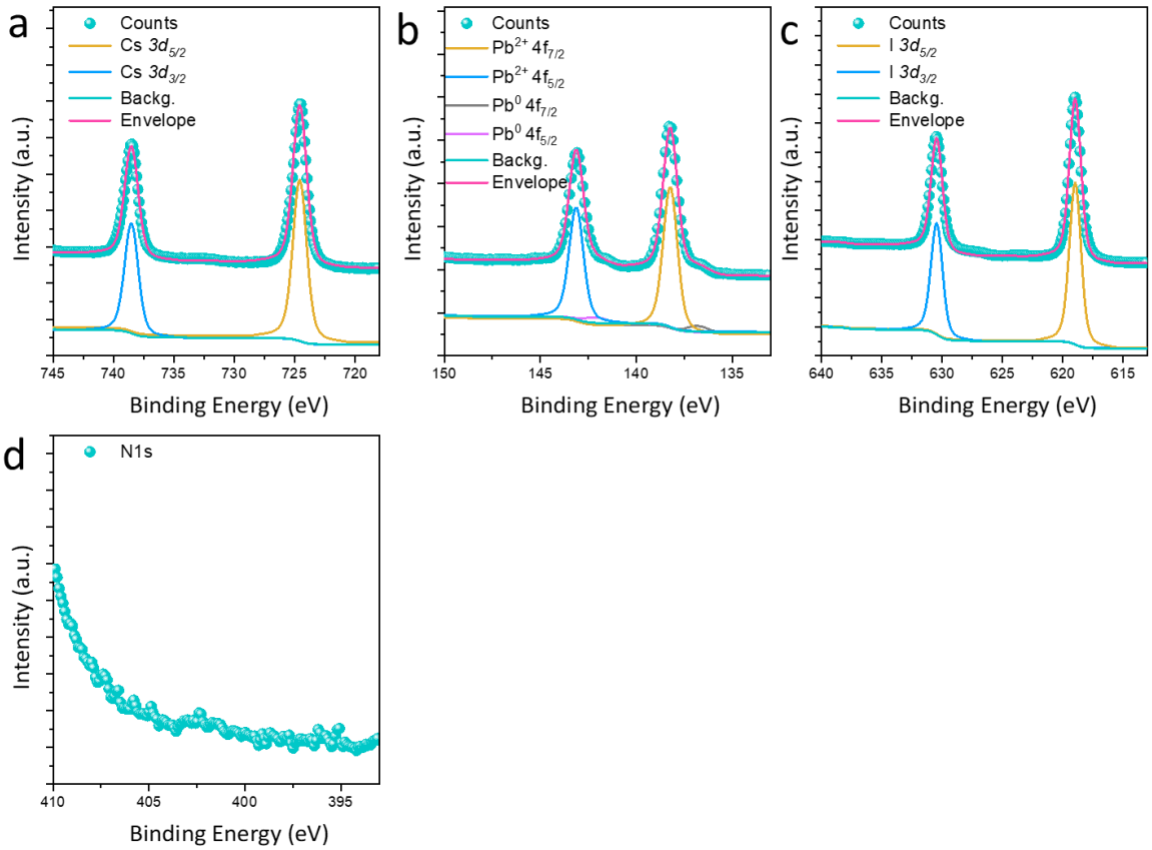

Supplementary Figure 18| a-d. XPS fittings for the Cs 3d, Pb 4f, I 3d and N 1s core levels for the controlled γ–$CsPbI_3$ sample. The counts and envelope (fit) have been offset to make the fittings clearer. Full details of peak positions can be found in **Supplementary Table 4**.

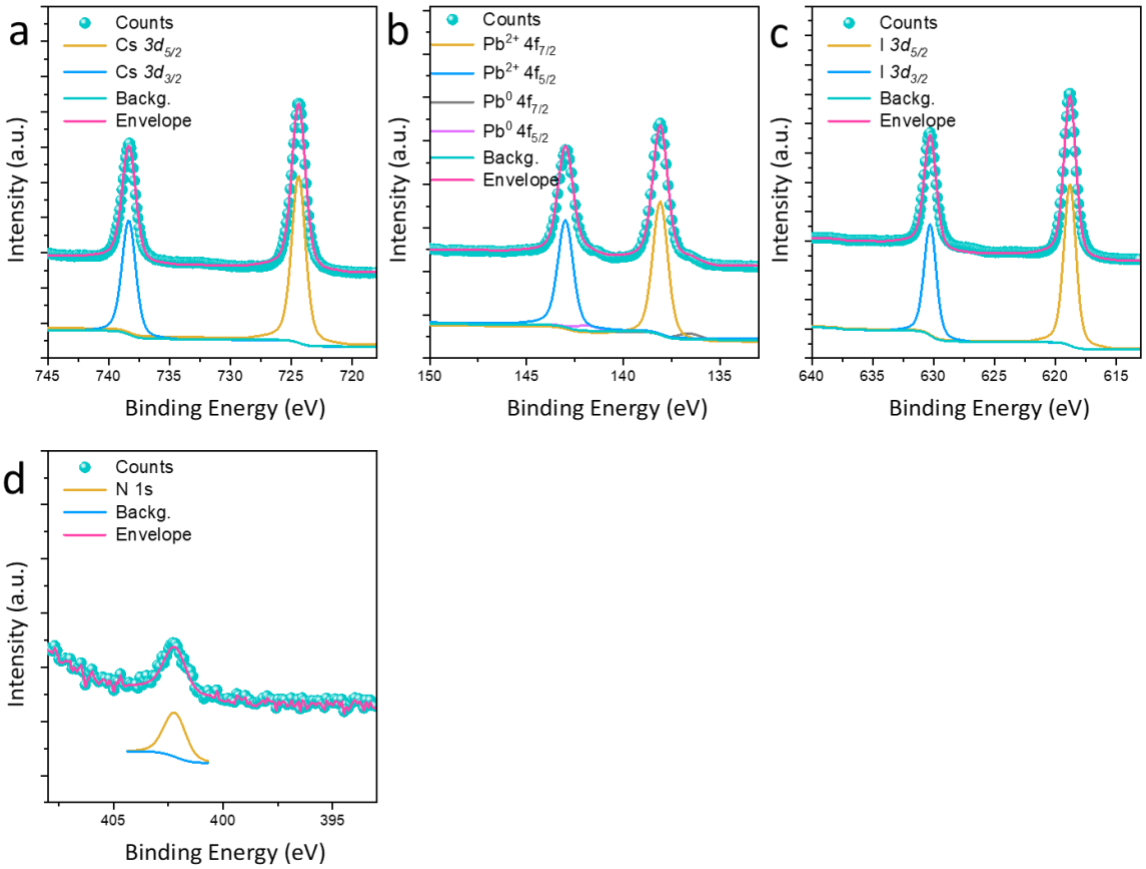

Supplementary Figure 19| a-d. XPS fittings for the Cs 3d, Pb 4f, I 3d, and N 1s core levels for the controlled γ–$CsPbI_3$-GAI sample. The counts and envelope (fit) have been offset to make the fittings clearer. Full details of peak positions can be found in **Supplementary Table 4**.

Supplementary Table 3. XPS core-level peak positions of hot-air processed β–$CsPbI_3$, and β–$CsPbI_3$-$Zn(C_6F_5)_2$ thin films.

Perovskites	β–**$CsPbI_3$**			β–**$CsPbI_3$-$Zn(C_6F_5)_2$**		
Core levels	**Start BE (eV)**	**Peak BE (eV)**	**End BE (eV)**	**Start BE (eV)**	**Peak BE (eV)**	**End BE (eV)**
Cs $3d_{5/2}$	751.19	724.17	715.44	751.85	724.33	715.74
Cs $3d_{3/2}$	751.19	738.11	715.44	751.85	738.27	715.74
Pb $4f_{7/2}$	155.44	136.57	130.44	155.74	136.64	130.74
Pb0	155.44	137.96	130.44	155.74	138.04	130.74
Pb $4f_{5/2}$	155.44	141.87	130.44	155.74	141.94	130.74
Pb 0	155.44	142.86	130.44	155.74	142.94	130.74
I $3d_{5/2}$	640.44	618.66	610.44	640.74	618.78	610.74
I $3d_{3/2}$	640.44	630.13	610.44	640.74	630.25	610.74
N 1s	-	-	-	-		
Zn $2p_{1/2}$	-	-	-	1051	1041.9	1040
Zn $2p_{3/2}$				1028	1027.74	1017
F 1s	-	-	-	691	683.22	681

Supplementary Table 4. XPS core-level peak positions of thermally evaporated γ–$CsPbI_3$, and γ–$CsPbI_3$-GAI thin films.

Perovskites	γ–**$CsPbI_3$**			γ–**$CsPbI_3$-GAI**		
Core levels	**Start BE (eV)**	**Peak BE (eV)**	**End BE (eV)**	**Start BE (eV)**	**Peak BE (eV)**	**End BE (eV)**
Cs $3d_{5/2}$	752.9	724.58	716.03	752.61	724.4	715.88
Cs $3d_{3/2}$	752.9	738.51	716.03	752.61	738.33	715.88
Pb $4f_{7/2}$	156.03	136.83	131.03	155.88	136.6	130.88
Pb0	156.03	138.22	131.03	155.88	138.08	130.88
Pb $4f_{5/2}$	156.03	142.12	131.03	155.88	141.9	130.88
Pb0	156.03	143.12	131.03	155.88	142.98	130.88
I $3d_{5/2}$	641.03	618.97	611.03	640.88	618.8	610.88
I $3d_{3/2}$	641.03	630.45	611.03	640.88	630.28	610.88
N 1s	-	-	-	404.38	402.2	400.68
Zn 2p	-	-	-			
F 1s	-	-	-			

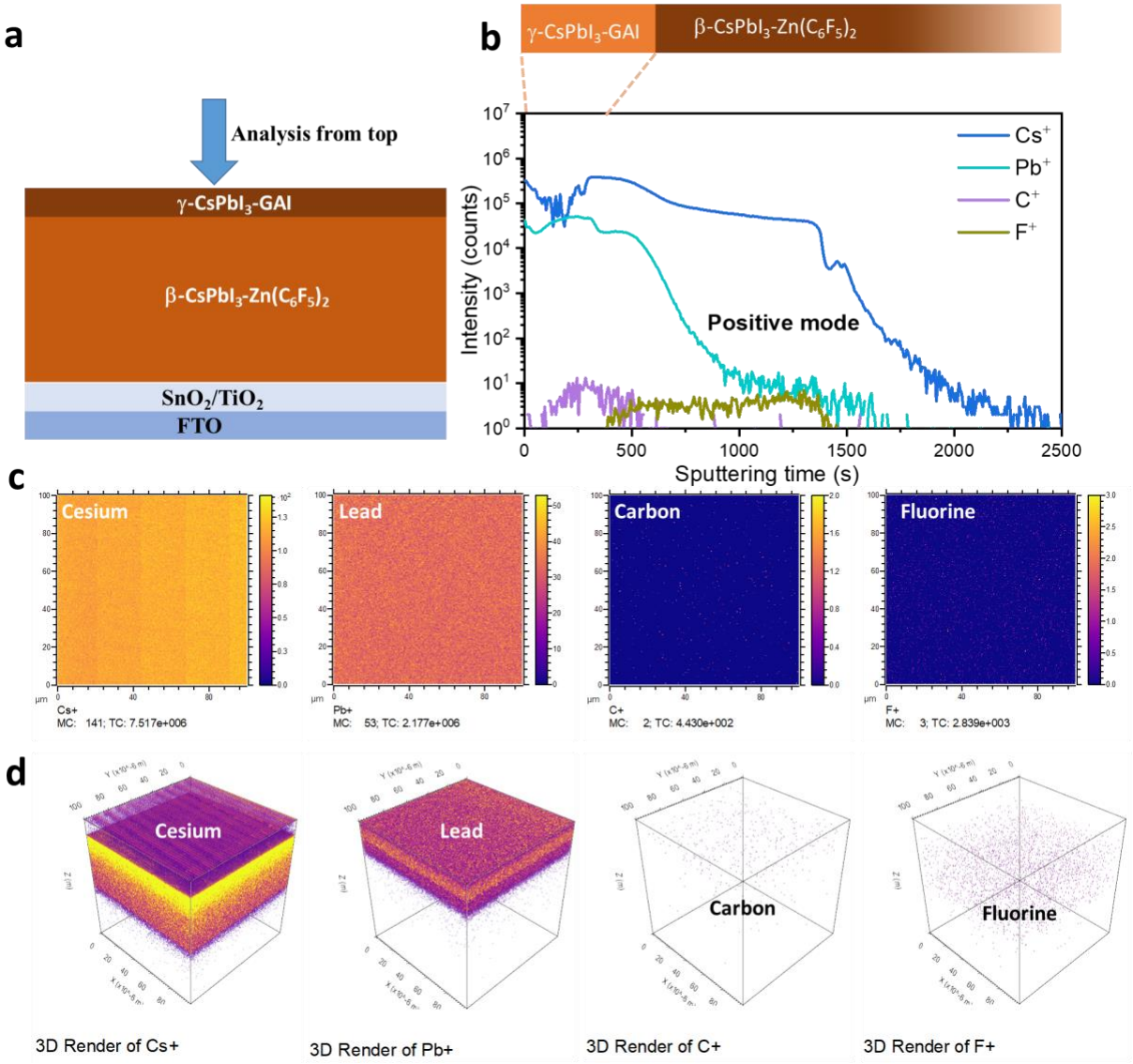

Supplementary Figure 20| ToF:SIMS elemental depth profiles of PHS thin film in positive mode. **a.** Schematic representation of experimental measurements used for β-$CsPbI_3$ + $Zn(C_6F_5)_2$ /γ-$CsPbI_3$-GAI thin film in positive mode. **b.** ToF:SIMS depth profiles. **c.** 2D images and **d.** 3D render images for Cs^+, Pb^+, C^+ and F^+ elements.

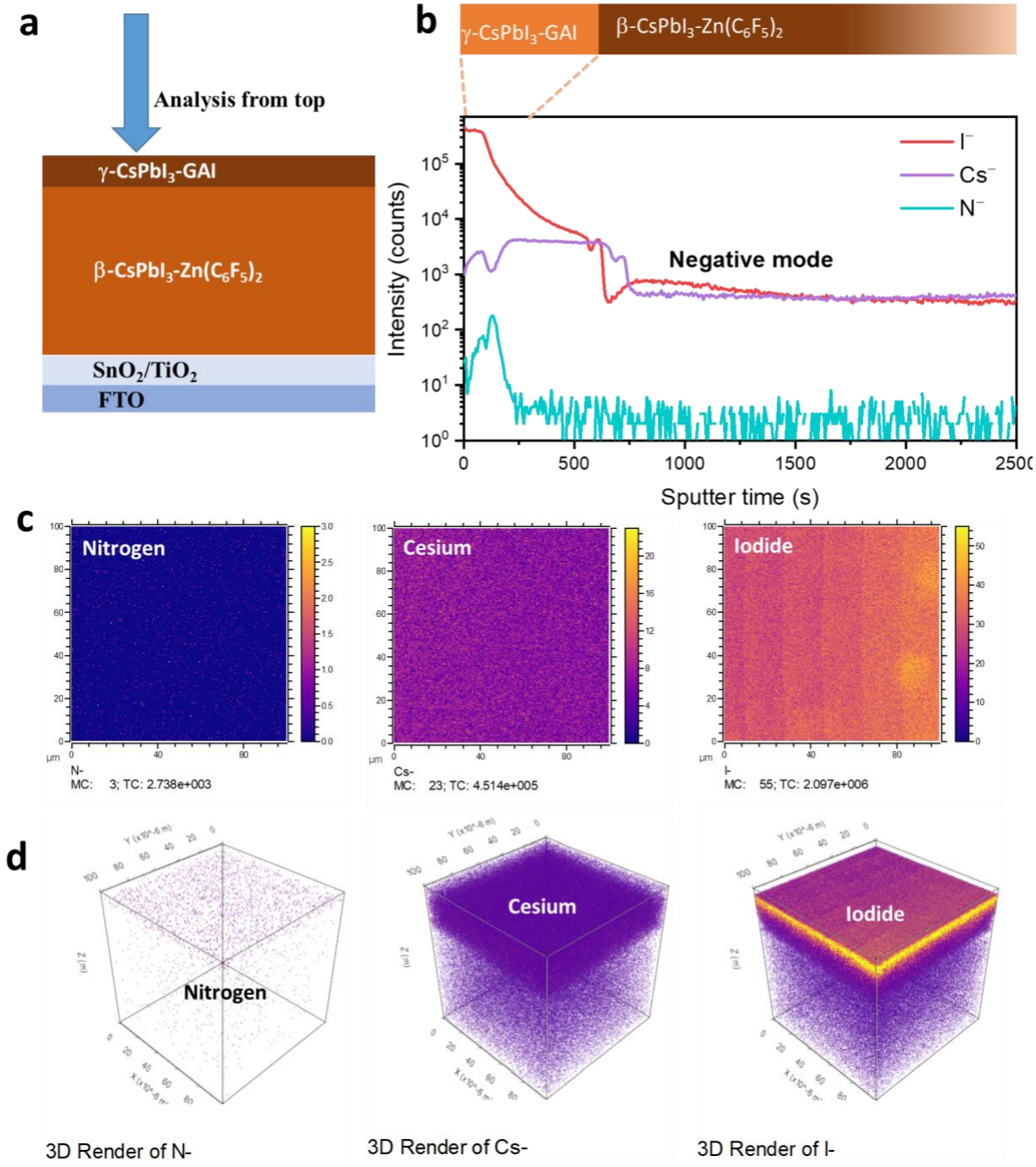

Supplementary Figure 21| ToF:SIMS elemental depth profiles of PHS thin film in negative mode. a. Schematic representation of experimental measurements used for β-$CsPbI_3$ + $Zn(C_6F_5)_2$ /γ-$CsPbI_3$-GAI thin film in negative mode. **b.** ToF:SIMS depth profiles of β-$CsPbI_3$ + $Zn(C_6F_5)_2$ /γ-$CsPbI_3$-GAI thin film in negative mode. **c.** 2D images and **d.** 3D render images for N^-, I^- and Cs^- elements.

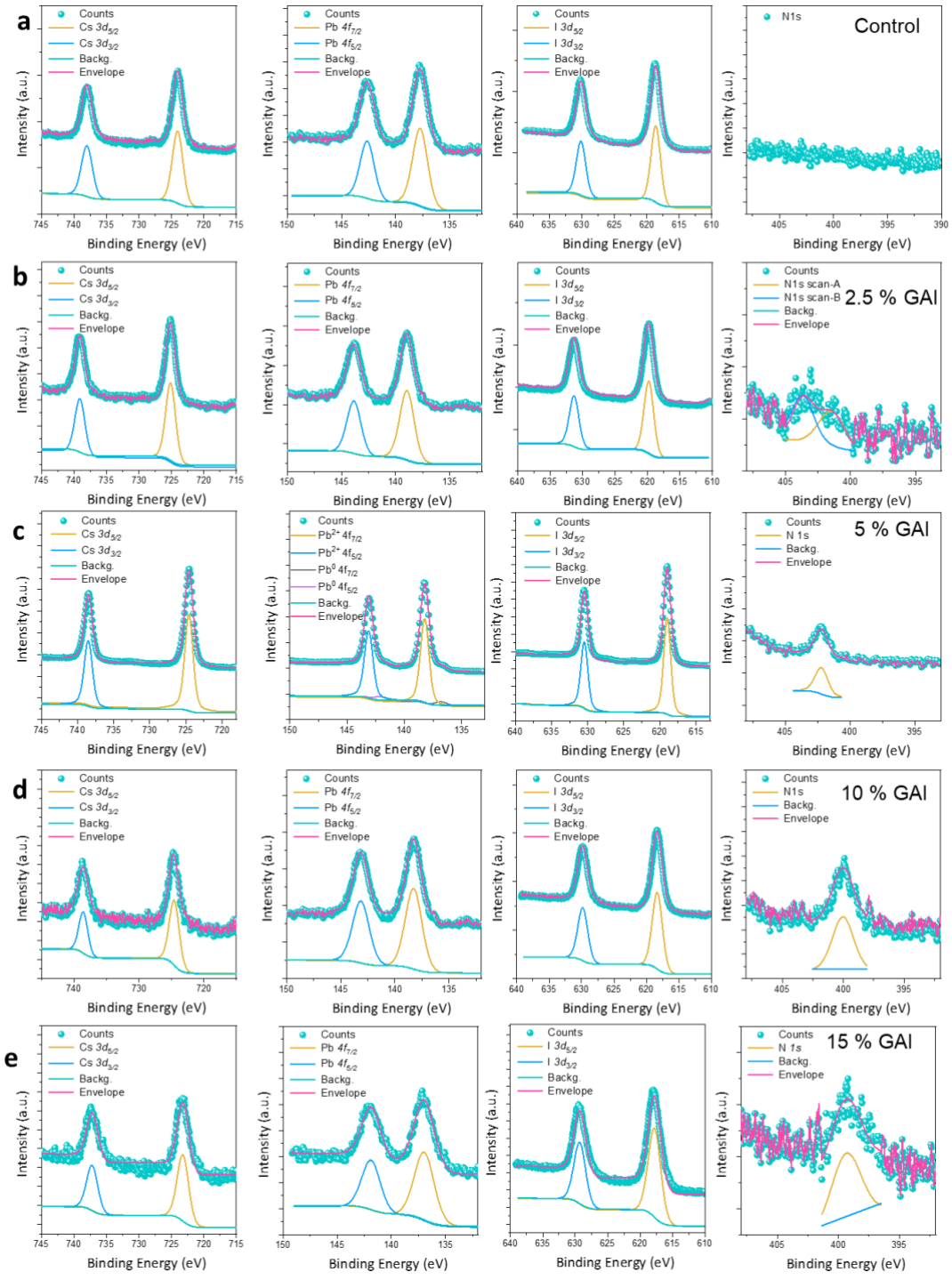

Supplementary Figure 22| a-e. XPS fittings for the Cs 3d, Pb 4f, I 3d and N 1s core levels for the controlled γ–$CsPbI_3$-GAI sample. The counts and envelope (fit) have been offset to make the fittings clearer. Atomic % of elements measured from XPS is summarized in **Supplementary Table 5**.

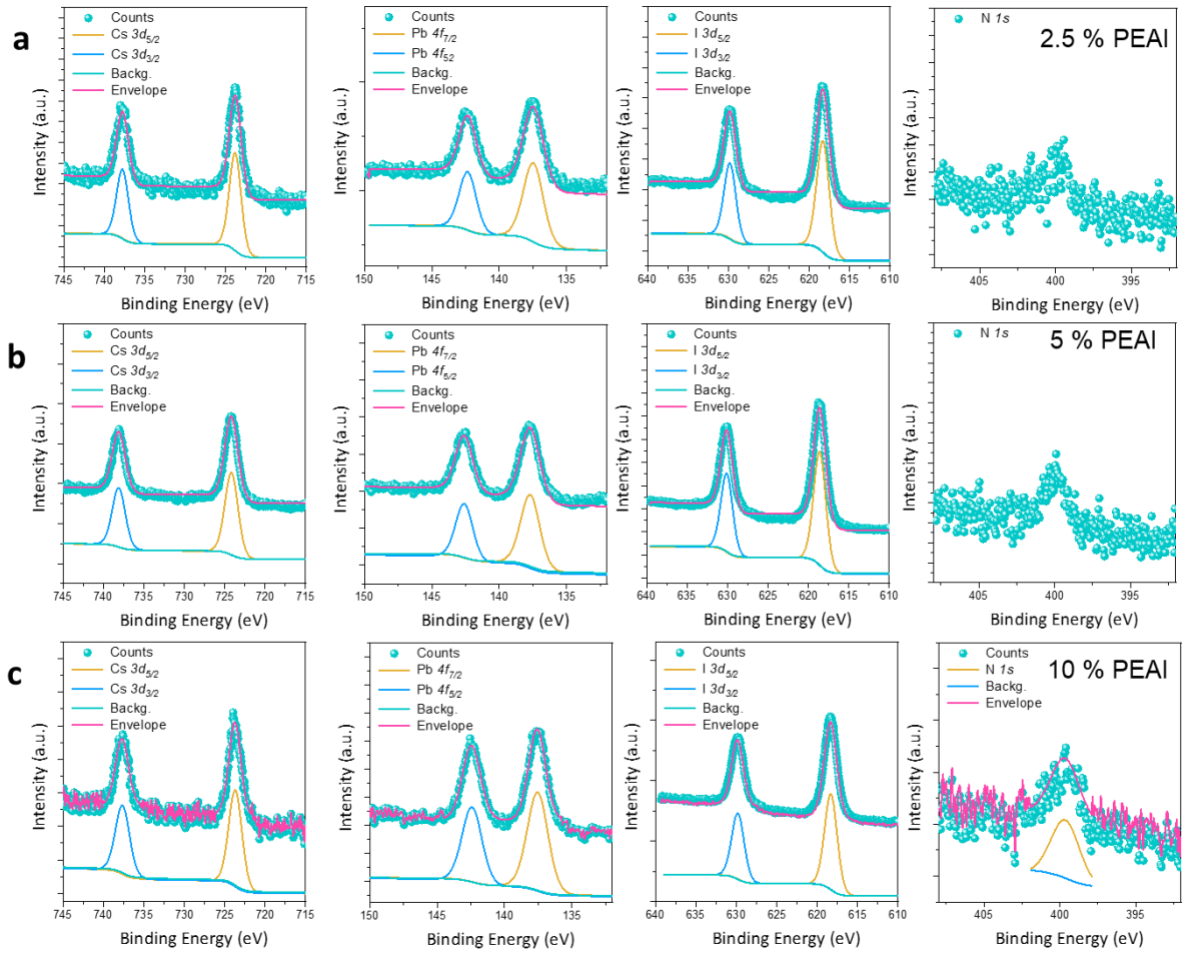

Supplementary Figure 23| a-e. XPS fittings for the Cs 3d, Pb 4f, I 3d and N 1s core levels for the controlled γ–$CsPbI_3$-PEAI sample. The counts and envelope (fit) have been offset to make the fittings clearer. Atomic percentage (%) of elements measured from XPS is summarized in **Supplementary Table 6**.

Supplementary Table 5. Atomic percentage (%) of elements measured at the surface of γ-$CsPbI_3$-GAI perovskite films with different GAI ratio.

GAI at. % XPS ⟶ / Expt. Used ↓	Cs	Pb	I	C	N
0	20.84	11.98	47.11	20.07	0
GAI:2.5	24.26	11.67	40.81	20.64	2.63
GAI:5	23.31	12.56	40.37	19.38	4.38
GAI:10	19.13	10.43	38.75	21.76	9.93
GAI:15	18.23	10.32	30.48	26.81	14.16

Supplementary Table 6. Atomic percentage (%) of elements measured at the surface of γ-$CsPbI_3$-PEAI perovskite films with different GAI ratio.

PEAI at. % XPS ⟶ / Expt. Used ↓	Cs	Pb	I	C	N
PEAI:2.5	23.62	11.47	41.48	20.85	2.58
PEAI:5	21.26	12.42	42.79	17.81	5.72
PEAI:10	19.58	11.85	39.56	16.43	12.58

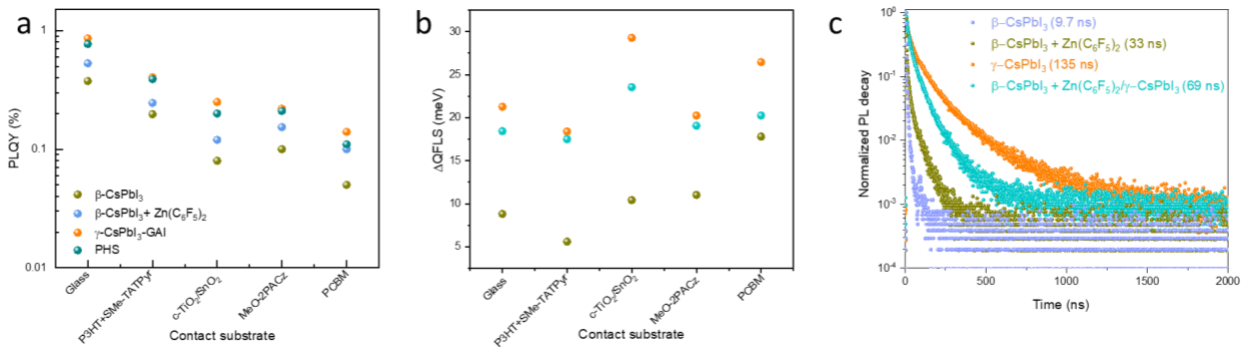

Supplementary Figure 24| a. PLQY analysis of perovskite thin films. **b.** Improvement in QFLS as determined by supplementary equation 1 for the respective samples. **c.** Time-resolved photoluminescence (TRPL) analysis of β–$CsPbI_3$ and γ–$CsPbI_3$ perovskite thin films deposited on glass substrates.

Supplementary Note 1.

PLQY discussion.

For a standard PV material, the change in QFLS following passivation (ΔQFLS = $QFLS_{modified}$–$QFLS_{control}$) is given by:[1, 2]

$$\Delta QFLS = 25.7meV \times \ln\left(\frac{PLQY_{modified}}{PLQY_{control}}\right) \quad \text{..... (Supplementary equation 1)}$$

From Supplementary equation 1 we can easily calculate the expected increase in open-circuit voltage for a given PLQY ratio.

The above Supplementary equation 1 can be modified to calculate the bandgap-independent loss from the radiative limit. By setting $PLQY_{modified}$ sample to be unity, i.e., in the ideal case, and then inputting the measured PLQY ($PLQY_{absolute}$), we obtain

$$\Delta QFLS_{rad} = 25.7meV \times \ln\left(\frac{1}{PLQY_{absolute}}\right) \quad \text{..... (Supplementary equation 2)}$$

where $PLQY_{absolute}$ is expressed in measured absolute value.

Supplementary Note 2.
TRPL discussion.

Time-resolved photoelectron (TRPL) spectroscopy analysis:

The obtained TRPL lifetime parameters were well fitted with a tri-exponential decay function from Supplementary equation 3. [3, 4]

$$I(t) = I_0 + A_1 \exp\left(-\frac{t-t_0}{\tau_1}\right) + A_2 \exp\left(\frac{-t-t_0}{\tau_2}\right) + A_3 \exp\left(\frac{-t-t_0}{\tau_3}\right) \quad \text{(Supplementary equation 3)}$$

Where, τ_1, τ_2 and τ_3 are first, second and third-order decay time, A_1, A_2 and A_3 are respective weight factors of each decay channel. Here, τ_1 stands for the fast decay lifetime and τ_2 and τ_3 stand for the slow decay function. The average lifetimes $<\tau_{avg}>$ of inorganic perovskite thin films were calculated from Supplementary equation 4. [3, 4]

$$<\tau_{avg}>=\sum_n \frac{\Sigma A_n \tau_n^2}{\Sigma_m A_m \tau_m^2} \quad \text{(Supplementary equation 4)}$$

The carrier transfer behavior of the β–$CsPbI_3$ and γ–$CsPbI_3$ films in contact with each other was well reflected in the carrier decay lifetime extracted from the time-resolved photoluminescence (TRPL) spectra (**Supplementary Figure 24**c). The lifetime extracted for a β–$CsPbI_3$-$Zn(C_6F_5)_2$ film deposited on a glass substrate is much higher (τ_{ave} = 33 ns) than that measured for the control β–$CsPbI_3$ layer (τ_{ave} = 9.7 ns). This significantly increased charge carrier lifetime indicates trap passivation induced by the presence of $Zn(C_6F_5)_2$ in the β–$CsPbI_3$ film. We also used TRPL spectroscopy to investigate the impact of thermally evaporated γ–$CsPbI_3$ on the excitonic quality of perovskite films. The charge carriers are relatively long-lasting in the case of γ–$CsPbI_3$ films (τ_{ave}=135 ns), which reflects the quality of the thermal evaporation method, **(Supplementary Table 10**). However, once we deposited the same γ–$CsPbI_3$ layer onto the β–$CsPbI_3$-$Zn(C_6F_5)_2$ film, we observed a dramatic decrease in a lifetime (τ_{ave}=69 ns). This is a clear indication of effective electron extraction between interfaces due to the different conductivity types of the β–$CsPbI_3$-$Zn(C_6F_5)_2$ and γ–$CsPbI_3$ perovskite thin films.

Supplementary Table 7. PLQY values for β-$CsPbI_3$ and β-$CsPbI_3$ + $Zn(C_6F_5)_2$ thin films deposited on Glass, isolated p-type (P3HT + SM-TATPyr), p-type MeO-2PACz, n-type TiO_2/SnO_2 and n-type PCBM substrates.

Substrate	**PLQY (β-CsPbI3) (%)**	**ΔQFLS$_{rad}$ (β-CsPbI3) (meV)**	**PLQY(b-CsPbI3-Zn(C6F)2) (%)**	**ΔQFLS$_{rad}$ (β-CsPbI3) (meV)**	**ΔQFLS (meV)**
Glass	0.3757	143	0.5296	134	8.82
P3HT+SMe-TATPyr	0.1974	160	0.2456	154	5.61
c-TiO_2/SnO_2	0.08	183	0.12	172	10.42
MeO-2PACz	0.10	177	0.1536	166	11.03
PCBM	0.05	195	0.1	177	17.81

Supplementary Table 8. PLQY values for β-$CsPbI_3$ and γ-$CsPbI_3$-GAI thin films deposited on Glass, isolated p-type (P3HT + SM-TATPyr), p-type MeO-2PACz, n-type TiO_2/SnO_2 and n-type PCBM substrates.

Substrate	**PLQY (β-CsPbI3) (%)**	**ΔQFLS$_{rad}$ (β-CsPbI3) (meV)**	**PLQY (γ-CsPbI3) (%)**	**ΔQFLS$_{rad}$ (γ-CsPbI3) (meV)**	**ΔQFLS (meV)**
Glass	0.3757	143	0.8597	122	21.27
P3HT+SMe-TATPyr	0.1974	160	0.404	141	18.40
c-TiO_2/SnO_2	0.08	183	0.25	154	29.28
MeO-2PACz	0.10	177	0.22	157	20.26
PCBM	0.05	195	0.14	169	26.46

Supplementary Table 9. PLQY values for β-$CsPbI_3$ and PHS thin films deposited on Glass, P3HT + SM-TATPyr, MeO-2PACz, TiO_2/SnO_2 and PCBM substrates.

Substrate	**PLQY (β-CsPbI3) (%)**	**$\Delta QFLS_{rad}$ (β-CsPbI3) (meV)**	**$PLQY_{(PHS)}$ (%)**	**$\Delta QFLS_{rad\ (PHS)}$ (meV)**	**ΔQFLS (meV)**
Glass	0.3757	143	0.7697	125	18.43
P3HT+SMe-TATPyr	0.1974	160	0.39	142	17.50
c-TiO_2/SnO_2	0.08	183	0.20	159	23.55
MeO-2PACz	0.10	177	0.21	158	19.07
PCBM	0.05	195	0.11	175	20.26

Supplementary Table 10. TRPL lifetime measurements of inorganic perovskite absorber layers. Weight fraction calculated from amplitude at particular lifetime decay.

Perovskite	**τ_1**	**τ_2**	**τ_3**	**A_1**	**A_2**	**A_3**	**$<\tau_{avg}>$**
β-$CsPbI_3$	1.1	6.6	63	0.8605	0.1357	0.038	9.7
β-$CsPbI_3$-$Zn(C_6F_5)_2$	1.4	12	71	0.7860	0.1834	0.0306	33
γ-$CsPbI_3$-GAI	13	87	296	0.5471	0.3998	0.0531	135
PHS	13	62	267	0.5952	0.3930	0.0118	69

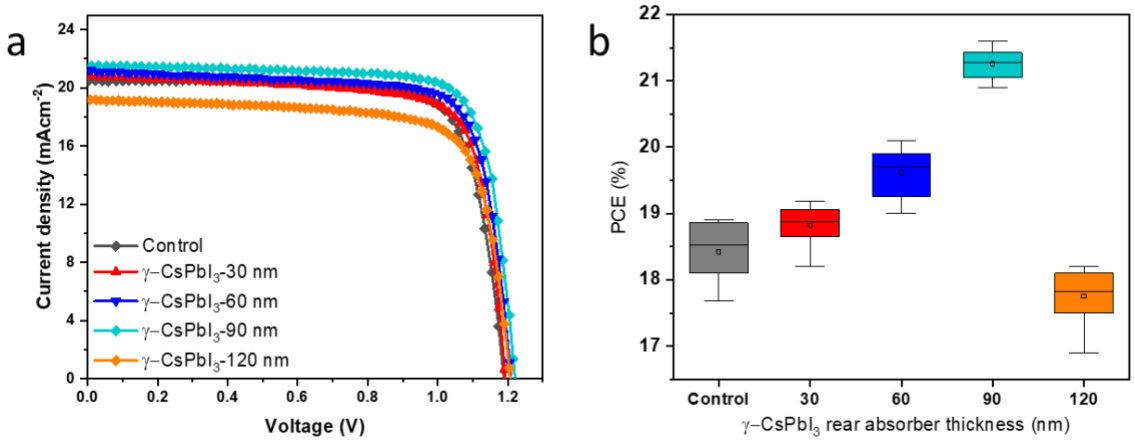

Supplementary Figure 25| Photovoltaic properties. a. J-V characteristics PHS based on different thicknesses of γ–$CsPbI_3$-GAI rear absorber. **b.** PCE distribution histograms of the cells with single junction and different PHS. The box plot in b displays the median line, mean, 25 %~75% box limits range within 1.5× interquartile range outlier whiskers. Twenty devices were tested respectively for control, 30, 60, 90 and 120 nm rear γ-$CsPbI_3$-GAI-based PHS devices.

Supplementary Table 11. Summary of solar cell parameters fabricated based on different thicknesses of rear γ–$CsPbI_3$ perovskites.

Front absorber (solution process)	**Rear absorber (thermal Evaporation)**	**γ–$CsPbI_3$-GAI Thickness (nm)**	**V_{OC} (V)**	**J_{SC} ($mAcm^{-2}$)**	**FF (%)**	**PCE (%)**
β–$CsPbI_3$-$Zn(C_6F_5)_2$	γ–$CsPbI_3$-GAI	0	1.187	20.50	77.5	18.86
		30	1.197	20.68	77.5	19.18
		60	1.209	20.98	79.23	20.09
		90	**1.220**	**21.72**	**81.5**	**21.59**
		120	1.209	19.18	78.09	18.10

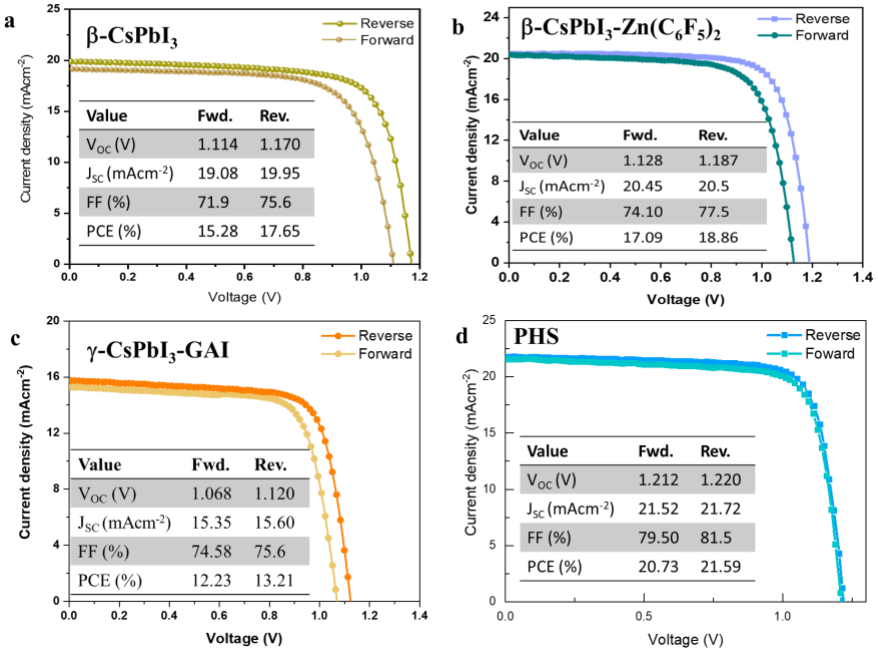

Supplementary Figure 26| Hysteresis analysis of champion PCS fabricated based on different absorbers. a. β-$CsPbI_3$ single junction **b.** β-$CsPbI_3$-$Zn(C_6F_5)_2$ single junction **c.** thermally evaporated γ-CsPbI3-GAI single junction and **d.** β-$CsPbI_3$-$Zn(C_6F_5)_2$/**γ**-$CsPbI_3$-GAI-based PHS device under forward and reverse scan.

Supplementary Table 12. Hysteresis analysis of champion perovskite solar cells fabricated based on different absorbers.

Perovskite absorber	**Scan direction**	**V_{OC} (V)**	**J_{SC} ($mAcm^{-2}$)**	**FF (%)**	**PCE (%)**	**HI**
β-$CsPbI_3$	Forward	1.114	19.08	71.9	15.28	0.134
	Reverse	1.170	19.95	75.6	17.65	
β-$CsPbI_3$-$Zn(C_6F_5)_2$	Forward	1.128	20.45	74.10	17.09	0.0938
	Reverse	1.187	20.5	77.5	18.86	
γ-$CsPbI_3$-GAI	Forward	1.068	15.35	74.58	12.23	0.0741
	Reverse	1.120	15.60	75.6	13.21	
PHS	Forward	1.212	21.52	79.50	20.73	0.0398
	Reverse	1.220	21.72	81.50	21.59	

Supplementary Table 13. Summary of solar cell parameters of reported inorganic PSCs based on different perovskite polymorphs and device configurations.

Sr. No.	Composition	Phase	Conf.	V_{OC} (V)	J_{SC} ($mAcm^{-2}$)	FF (%)	PCE (%)	Reference
α-$CsPbI_3$ n-i-p and p-i-n configuration including quantum dots.								
1	$CsPbI_3$	α-Phase	n-i-p	0.8	12	-	2.9	[5]
2	$CsPbI_3$ QDs	α-Phase	n-i-p	1.23	13.47	65	10.77	[6]
3	$CsPbI_3$	α-Phase	p-i-n	1.08	14.9	70	11.4	[7]
4	$CsPbI_3$	α-Phase	n-i-p	1.15	14.53	0.71	11.86	[8]
5	$CsPbI_3$ QDs	α-Phase	n-i-p	1.162	15.24	76.63	13.43	[9]
6	$CsPbI_3$	α-Phase	n-i-p	1.104	19.15	80.6	17.06	[10]
7	$CsPbI_3$ QDs	α-Phase	n-i-p	1.06	17.77	75.8	14.32	[11]
8	$CsPbI_3$	α-Phase	n-i-p	1.06	20.56	77.61	16.9	[12]
9	$CsPbI_3$ QDs	α-Phase	n-i-p	1.27	17.80	73.1	16.53	[13]
β–$CsPbI_3$ p-i-n configuration								
10	$CsPbI_3$	β-Phase	p-i-n	1.12	15.81	75.19	13.32	[14]
11	$CsPbI_{3-x}Br_x$	β-Phase	p-i-n	1.16	17.70	78.60	16.10	[15]
12	$CsPbI_3$	β-Phase	p-i-n	1.12	20.67	81.98	19.00	[16]
13	$CsPbI_3$	β-Phase	p-i-n	1.176	20.10	80.04	18.93	[17]
14	$CsPbI_3$	β-γ-Phase	p-i-n	1.160	20.64	84.17	20.17	[18]
15	**$CsPbI_3$**	**β-γ-Phase**	**p-i-n**	**1.148**	**20.75**	**79.9**	**19.03**	**[19]** **This work**
β–$CsPbI_3$ n-i-p configuration								
16	$CsPbI_3$	β-Phase	n-i-p	1.11	20.23	82.00	18.40	[20]
17	$CsPbI_{3-x}Br_x$	β-Phase	n-i-p	1.23	18.30	82.58	18.64	[21]
18	$CsPbI_3$	β-Phase	n-i-p	1.13	20.23	82.70	19.03	[22]
19	$CsPbI_3$	β-Phase	n-i-p	1.07	20.08	77.32	16.67	[23]
20	$CsPbI_3$	β-Phase	n-i-p	1.12	20.25	80.50	18.27	[24]

21	$CsPbI_{2.85}Br_{0.15}$	β-Phase	n-i-p	1.23	19.94	80.11	19.65	[25]
22	$CsPbI_3$	β-Phase	n-i-p	1.15	20.76	84.30	20.08	[26]
23	$CsPbI_3$	β-Phase	n-i-p	1.20	20.59	82.50	20.37	[27]
24	$CsPbI_3$	β-Phase	n-i-p	1.17	20.52	83.40	20.04	[28]
25	$CsPbI_3$	β-Phase	n-i-p	1.20	20.68	81.87	20.32	[29]
26	**$CsPbI_3$**	**β-γ-Phase**	n-i-p	**1.220**	**21.72**	**81.5**	**21.59**	**[30]**
								This work
γ–$CsPbI_3$ p-i-n configuration								
27	$CsPbI_3$	γ-Phase	p-i-n	0.93	14.3	68	8.84	[31]
28	$CsPbI_3$	γ-Phase	p-i-n	1.09	17.33	79.41	15	[32]
29	$CsPbI_3$	γ-Phase	p-i-n	1.172	20.58	78.84	19.01	[33]
γ–$CsPbI_3$ n-i-p configuration								
30	$CsPbI_3$	γ-Phase	n-i-p	0.79	0.26	45	0.09	[34]
31	$CsPbI_3$	γ-Phase	n-i-p	1.04	16.53	65.7	11.3	[35]
32	$CsPbI_3$	γ-Phase	n-i-p	1.059	18.95	74.9	15.07	[36]
33	$CsPbI_{3-x}Br_x$	γ-Phase	n-i-p	1.23	20.55	81.90	20.80	[37]
34	$CsPbI_3$	γ-Phase	n-i-p	1.182	18.67	83.38	18.41	[38]
35	$CsPbI_{3-x}Br_x$	γ-Phase	n-i-p	1.20	20.86	84.10	21.0	[39]
36	$CsPbI_3$	γ-Phase	n-i-p	1.244	20.60	82.52	21.15	[40]

Supplementary Table 14. Perovskite solar cell parameters fabricated using β–$CsPbI_3$-$Zn(C_6F_5)_2$ via the hot-air method. Device area for all samples was 0.3 x 0.3 cm^2 and J-V curves were measured under standard AM 1.5G (air mass 1.5 global) illumination.

Device No.	V_{OC} (V)	J_{SC} ($mAcm^{-2}$)	FF (%)	PCE (%)
1	1.169	19.55	75.65	17.29
2	1.168	19.25	75	16.86
3	1.165	19.92	75.68	17.56
4	1.165	20.35	76	18.02
5	1.156	20.25	74.8	17.51
6	1.153	20.5	76.9	18.18
7	1.165	20.15	77.8	18.26
8	1.166	20.45	77.42	18.46
9	1.158	20.36	74.6	17.59
10	1.170	19.68	76.58	17.63
11	1.168	19.85	74.6	17.30
12	1.177	20.1	75.8	17.93
13	1.165	20.35	76.08	18.04
14	1.165	20.45	75.9	18.08
15	1.18	20.15	76.5	18.19
16	1.187	20.5	77.5	18.86
17	1.175	20.3	77.3	18.44
18	1.168	20.2	77.5	18.29
19	1.171	20.25	75.7	17.95
20	1.168	20.48	76.2	18.23
Average	1.168±0.01	20.155±0.34	76.17±1	17.94±0.48

Supplementary Table 15. Perovskite solar cell parameters fabricated using γ–$CsPbI_3$-GAI via thermal evaporation method. Device area for all samples was 0.3 x 0.3 cm^2 and J-V curves were measured under standard AM 1.5G (air mass 1.5 global) illumination.

Device No.	V_{OC} (V)	J_{SC} ($mAcm^{-2}$)	FF (%)	PCE (%)
1	1.11	15.62	73.5	12.74
2	1.115	15.32	74.0	12.64
3	1.12	15.4	75.6	13.04
4	1.10	14.6	77.0	12.37
5	1.12	14.98	76.0	12.75
6	1.00	15.5	72.0	11.16
7	0.98	15.6	73.5	11.24
8	1.105	13.98	76.0	11.74
9	1.108	14.85	75.5	12.42
10	1.108	15.0	75.5	12.55
11	1.105	15.2	75.4	12.66
12	1.12	15.2	75.8	12.90
13	1.12	16.0	76.08	13.63
14	1.12	15.6	75.6	13.21
15	1.115	15.2	76.5	12.97
16	1.117	16.0	77.58	13.87
17	1.104	15.8	75.6	13.19
18	1.12	15.4	74.1	12.76
19	1.18	14.3	75.8	12.79
20	1.116	15.3	77.1	13.15
Average	1.105±0.042	15.25±0.52	75.30±1.36	12.70 ±0.68

Supplementary Table 16. Perovskite solar cell parameters fabricated using β–$CsPbI_3$-$Zn(C_6F_5)_2$ /γ–$CsPbI_3$-GAI-based PHS devices. Device area for all samples was 0.3 x 0.3 cm^2 and J-V curves were measured under standard AM 1.5G (air mass 1.5 global) illumination.

Device No.	V_{OC} (V)	J_{SC} ($mAcm^{-2}$)	FF (%)	PCE (%)
1	1.21	20.2	79.5	19.43
2	1.21	21.0	79.3	20.15
3	1.215	20.5	77.8	19.38
4	1.215	21.1	79.5	20.38
5	1.220	21.72	81.5	21.60
6	1.217	21.56	80.0	20.99
7	1.210	21.65	80.2	21.01
8	1.210	21.2	81.0	20.78
9	1.220	21.45	81.2	21.25
10	1.216	21.1	81.5	20.91
11	1.213	21.35	80.5	20.85
12	1.220	21.1	79.9	20.57
13	1.218	21.5	81.0	21.21
14	1.216	21.4	80.5	20.95
15	1.218	21.58	79.5	20.90
16	1.220	21.65	79.5	20.99
17	1.200	21.4	79.85	20.51
18	1.205	20.95	81.2	20.50
19	1.205	21.4	81.2	20.94
20	1.214	21.1	80.8	20.70
Average	1.214 ±0.007	21.25±0.34	80.25±1.1	20.70 ± 0.5

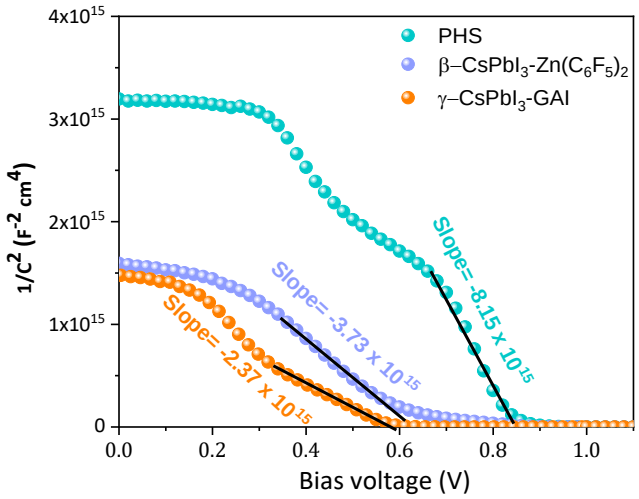

Supplementary Figure 27| MS curves of the control single junction β–$CsPbI_3$-$Zn(C_6F_5)_2$, γ–$CsPbI_3$, and PHS-based devices; the slope was obtained by fitting the linear part. The fitting lines are obtained by a linear fitting of data points.

Supplementary Note 3
Mott-Schottky (M-S) analysis

The $1/C^2$ versus voltage plots attained from the C-V measurements and the corresponding built-in potential and charge distribution at the perovskite/HTM interface were extracted by the Mott-Schottky equation. [41]

$$\frac{1}{C^2} = \frac{2}{A^2 e N_A \varepsilon_0 \varepsilon}(V_{bi} - V - \frac{2k_B T}{e}) \quad \text{----- (Supplementary equation 5)}$$

where C is the capacitance of the depletion-layer, A is the active area, e is the elementary charge, N_A is the carrier density, ε_0 is the vacuum permittivity, ε is the relative dielectric constant, V_{bi} is the built-in potential at equilibrium, V is the applied voltage, k_B is Boltzmann's constant, and T is the absolute temperature.

Therefore a plot of C^{-2} versus V yields a straight line with a slope than can be used to determine N_A.

$$Slope = \frac{2}{e\varepsilon_0 \varepsilon N_A A^2} \quad \text{….. (Supplementary equation 6)}$$

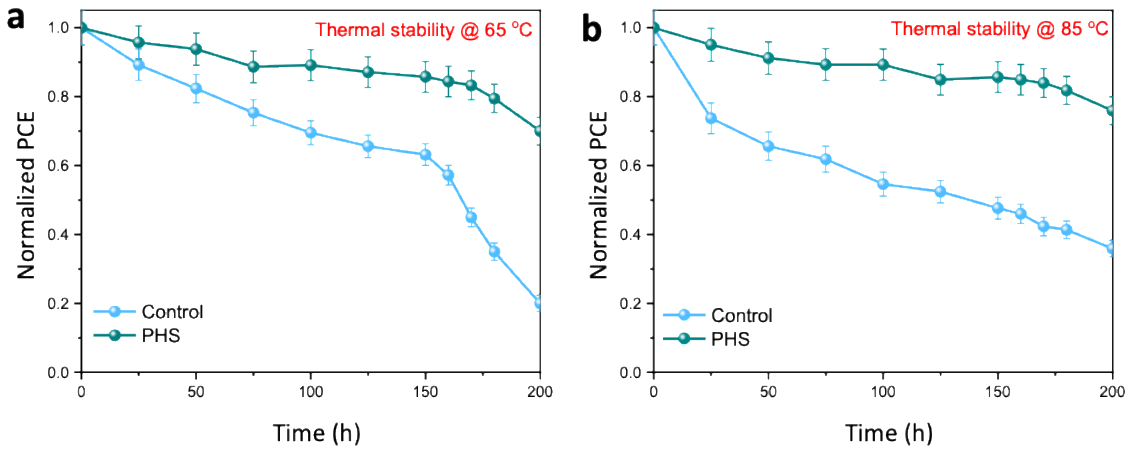

Supplementary Figure 28| Thermal stability analysis. Thermal stability tests of the control and PHS at **a.** 65 °C and **b.** 85 °C thermal stress without encapsulation. Data shows ± 5% error bar. Error bars represent the standard deviation of ten devices for control as well as for 90nm γ-CsPbI3-GAI PHS-based devices. Data are presented as mean values ± SD. For J-V measurements, devices were taken outside the glove box (every ~24 h) and immediately kept in the glove box after every J-V measurement. Relative humidity 20-25 % during measurements.

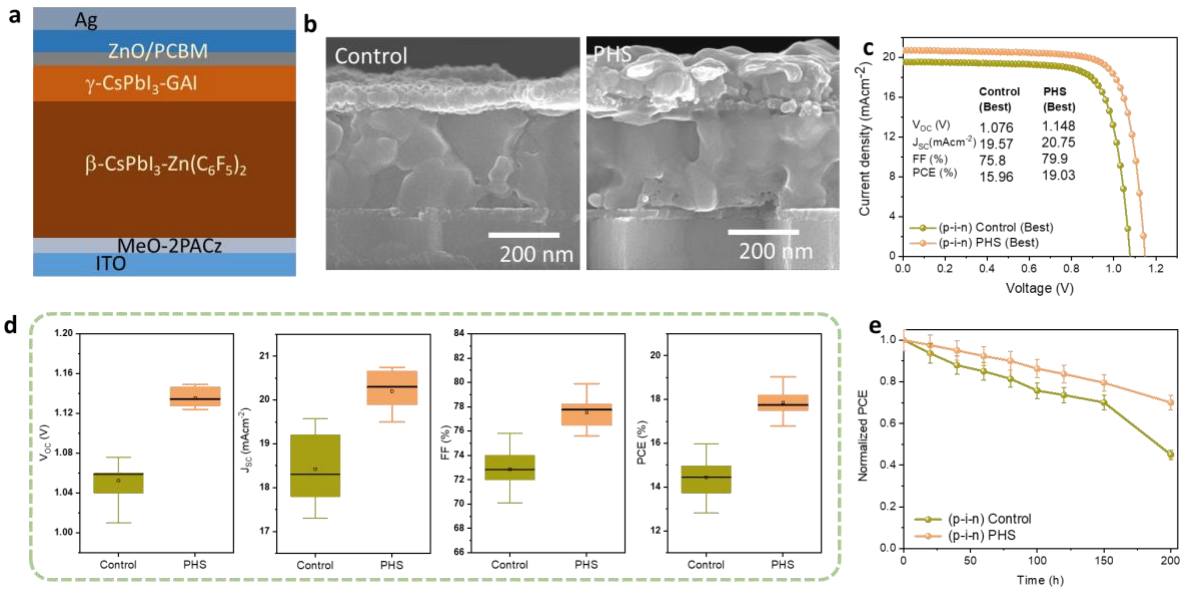

Supplementary Figure 29| Device configuration, cross-sectional view and J-V characterizations of inverted "p-i-n" type PHS-based devices. **a**. Device configuration of inverted p-i-n PHS. **b.** Cross-sectional SEM images of respected control and PHS-based complete device. **c**. J-V curves in reverse scans. **d**. detailed photovoltaic properties. Total of twenty devices were recorded in control and PHS configuration. The box plot in d panel displays the median line, mean, 25 %~75% box limits range within 1.5× interquartile range outlier whiskers. **e.** Stability is monitored in ambient conditions without encapsulation. Error bars (5%) represent the standard deviation of seven and ten devices for control and PHS respectively. Relative humidity 20-25 %. Data are presented as mean values ± SD. Seven and ten devices were monitored respectively for control, 90 nm γ-$CsPbI_3$ based PHS-based devices.

Supplementary Note 4

Towards hybrid phase heterojunction solar cells (H-PHS)

Generally speaking, the suitability of the developed method towards alternative perovskite compositions is equally important. For this, we further explore the feasibility of our PHS approach in alternative polymorphs of organic-inorganic hybrid perovskites phase heterojunction (H-PHS). However, this type of two different compositions is not pure phase heterojunction but heterojunction or bilayered or 3D/PP-2D bilayer perovskite device has been reported previously. [42, 43, 44] In this section, we implemented all-inorganic $CsPbI_2Br$ and organic-inorganic hybrid $MAPbI_3$, $Cs_{0.05}FA_{0.95}PbI_3$ perovskite composition in order to check PHS concept for alternative composition. For this, used γ-$CsPbI_2Br$ front absorber deposited by the dynamic hot-air (DHA) method in ambient conditions, [45] followed by thermal evaporation of α-$MAPbI_3$ or α-$Cs_{0.05}FA_{0.95}PbI_3$ rear absorber. These two different γ and α-phases were successfully deposited and analyzed by GIXRD and ToF-SIMS analyses, (**Supplementary Figure 20-27**). Furthermore, UPS analysis clearly revealed that VBM of the γ-$CsPbI_2Br$/α-$MAPbI_3$ and γ-$CsPbI_2Br$/α-$Cs_{0.05}FA_{0.95}PbI_3$ interfaces are aligned at the heterointerface, while CBM of γ-$CsPbI_2Br$ is lower than both α-phases of rear absorbers. In this scenario, once the light is shined on this phase-heterojunction, the photoexcited electrons are extracted towards the γ-$CsPbI_2Br$, while the holes remain in the α-phase. Therefore, there is a possibility for an additional charge transfer mechanism that can prevent this radiative recombination in the α-phase, resulting in the formation of a hybrid phase heterojunction solar cell (H-PHS) with gradient energy levels, (**Figure 28, Supplementary Table 19**). However, this study is out of scope in the present manuscript, but this is one of the simple demonstrations that the PHS concept can be implemented in the alternative compositions in halide perovskites.

Supplementary Table 17. Detailed thermal evaporation parameters for α–$Cs_{0.5}FA_{0.95}PbI_3$ individual materials for hybrid perovskite. * *Initial rate need to optimize carefully.*

Precursor	**PbI_2**	**CsI**	**FAI**
Set rate (Å/s)	0.7-0.8	0.1-0.05	0.6-0.7
Temperature (^oC)	310-330	445-455	150-160
Current required (Amp)	45-50	65-70	38-42*
Heating source	Q-Crucible		

Supplementary Table 18. Detailed thermal evaporation parameters for α–$MAPbI_3$ individual materials for hybrid perovskite. * *Initial rate needs to optimize carefully.*

Precursor	**PbI_2**	**MAI**
Set rate (Å/s)	0.7-0.8	0.6-0.7
Temperature (^oC)	310-330	120-125
Current required (Amp)	45-50	38-40*
Heating source	Q-Crucible	

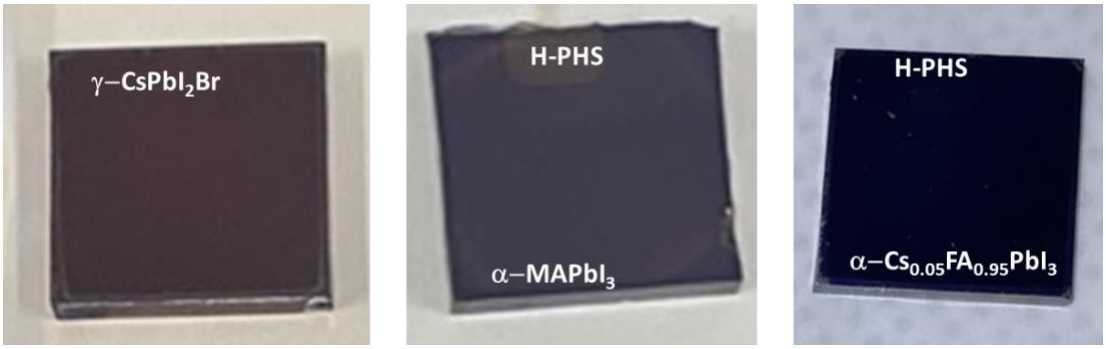

Supplementary Figure 30| Photographs of γ–$CsPbI_2Br$, γ–$CsPbI_2Br$/α–$MAPbI_3$ (H-PHS), and γ–$CsPbI_2Br$/α–$Cs_{0.05}FA_{0.95}PbI_3$ thin films and stored in ambient condition over 24 hours. Relative humidity 25-30 %.

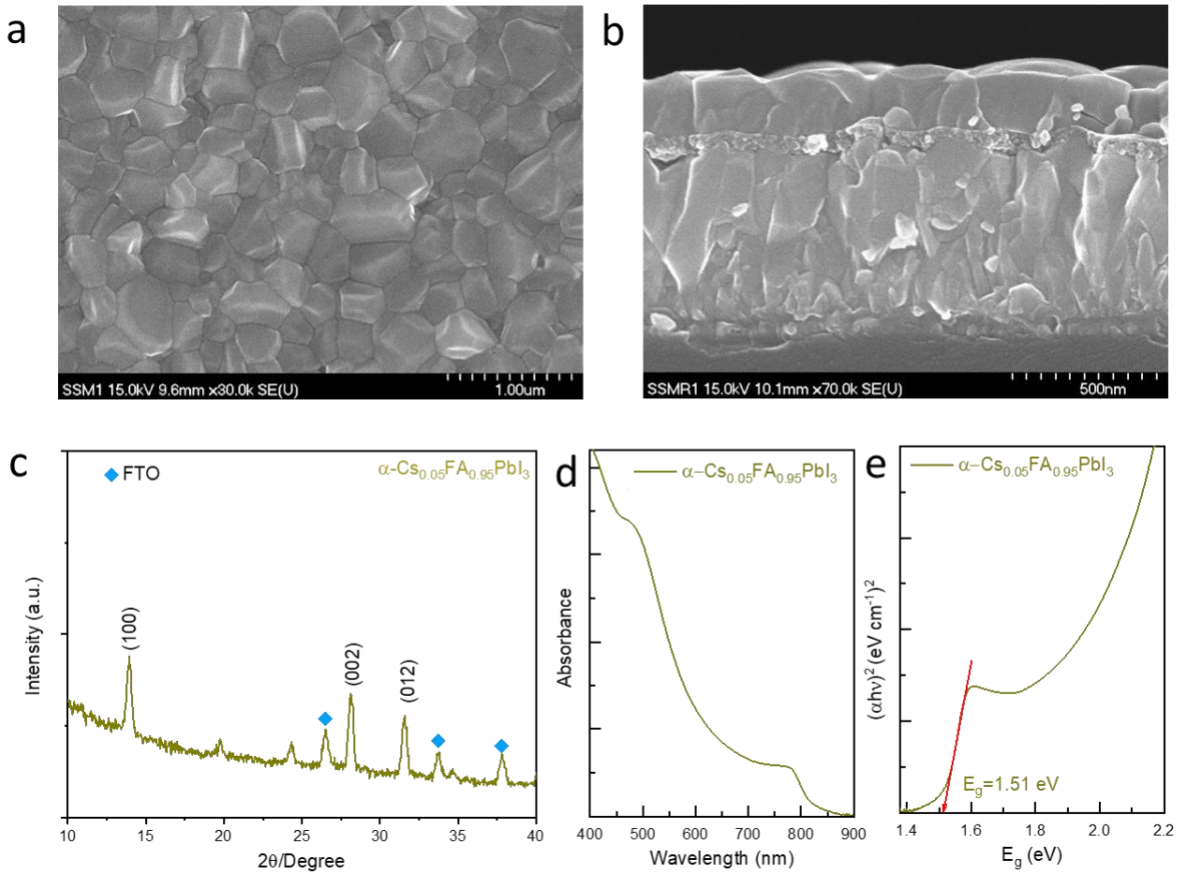

Supplementary Figure 31| Morphological, structural and optical properties of α–$Cs_{0.05}FA_{0.95}PbI_3$ perovskite thin film deposited by the triple source thermal evaporation method. The fitting lines in d-e were obtained by linear fitting of data points.

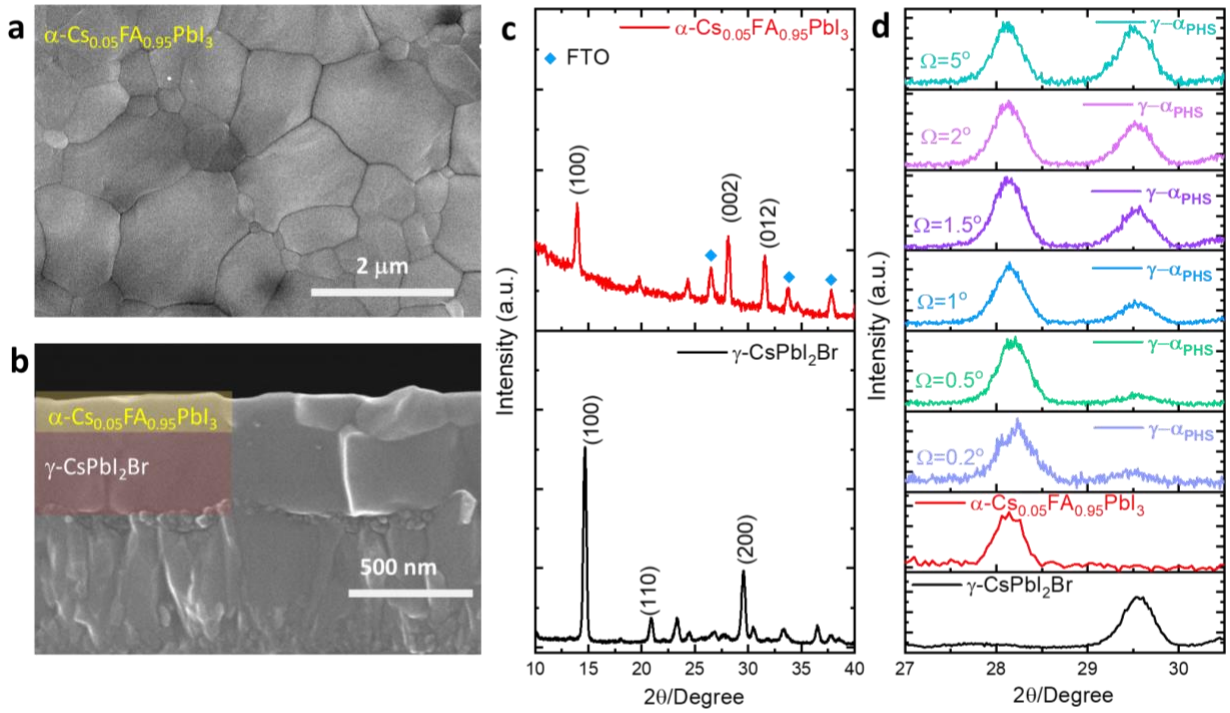

Supplementary Figure 32| Morphological, optical and structural properties of γ–$CsPbI_2Br$/ α-$Cs_{0.05}FA_{0.95}PbI_3$-based H-PHS devices. **a**. Top-view of α-$Cs_{0.05}FA_{0.95}PbI_3$ perovskite thin film deposited on γ–$CsPbI_2Br$ substrate. **b**. Cross-sectional SEM image of γ–$CsPbI_2Br$/α-$Cs_{0.05}FA_{0.95}PbI_3$-based hybrid phase-heterojunction (H-PHS) thin film. **c**. respective cross sectional view. **c.** The complete XRD patterns of individual γ–$CsPbI_2Br$ (*hot air method*) and α-$Cs_{0.05}FA_{0.95}PbI_3$ perovskite thin films (*thermal evaporation method*). **d**. structural properties of γ–$CsPbI_2Br$/α- $Cs_{0.05}FA_{0.95}PbI_3$–based H-PHS thin film recorded at a different incident angle (Ω).

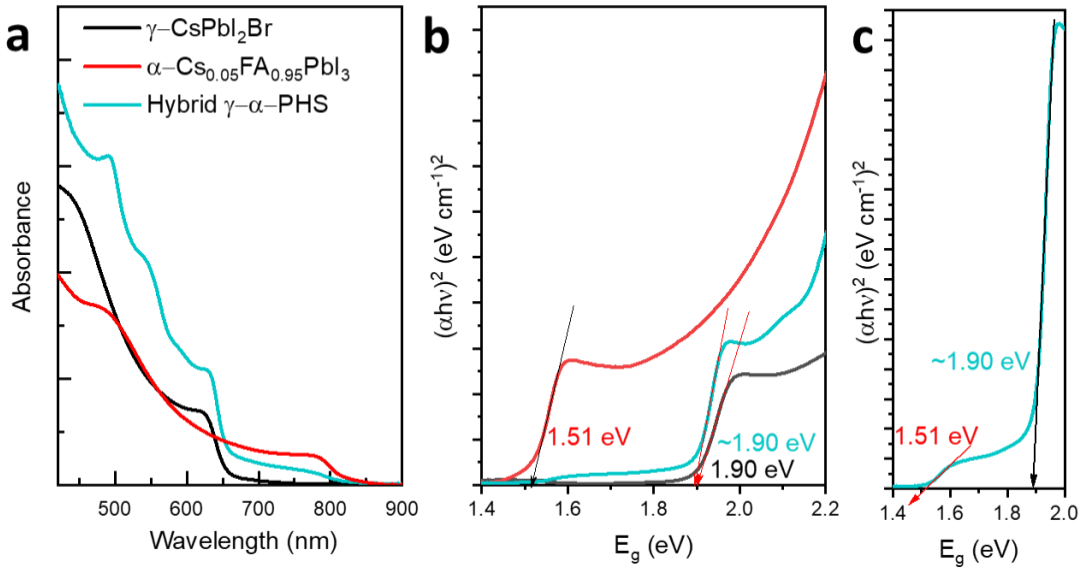

Supplementary Figure 33| Optical properties of the γ–$CsPbI_2Br$/α-$Cs_{0.05}FA_{0.95}PbI_3$-based H-PHS thin films. **a.** UV-Vis optical absorption of γ–$CsPbI_2Br$, **α**-$Cs_{0.05}FA_{0.95}PbI_3$ and H-PHS thin films. **b**. Tauc plots for respective samples. **c**. Magnified Tauc plot of H-PHS showing two independent phases in single H-PHS thin film. The fitting lines in b-c are obtained by a linear fitting of data points.

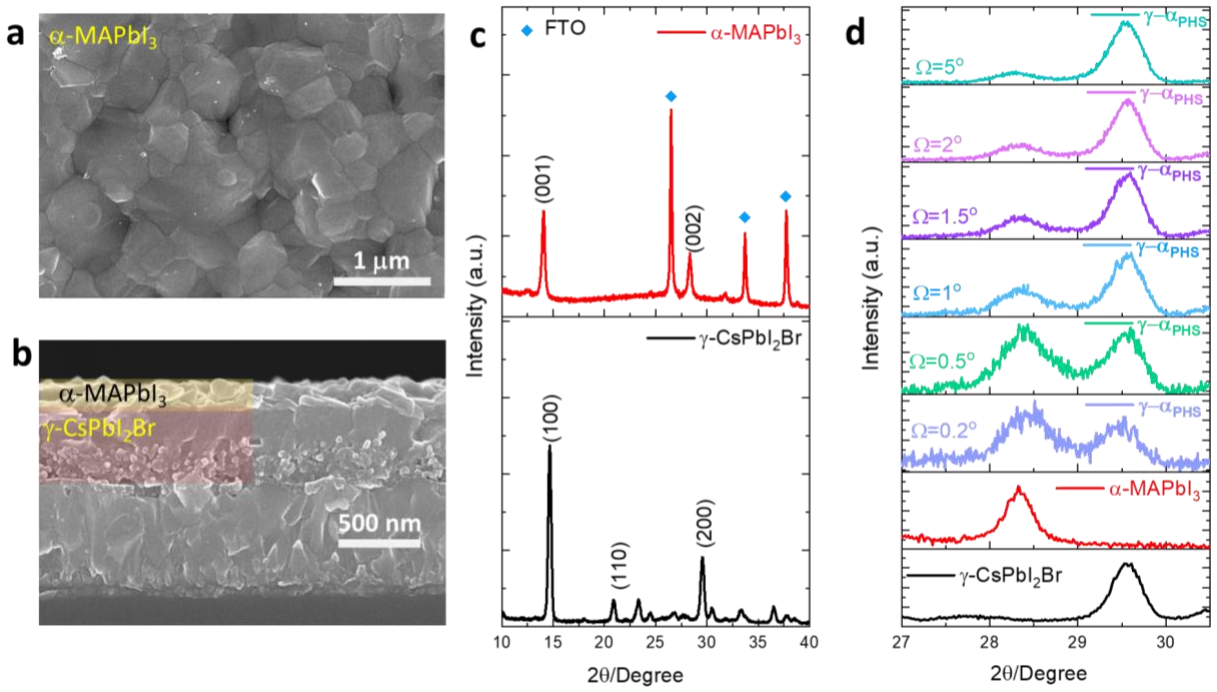

Supplementary Figure 34| Morphological, optical and structural properties of γ–$CsPbI_2Br$/ α-$MAPbI_3$-based H-PHS devices. γ–β-based alternative PHS device architecture. **a.** to-view SEM of α-$MAPbI_3$ thin film deposited on γ–$CsPbI_2Br$ substrate. **b.** respective cross-sectional view. **c.** The complete XRD patterns of individual γ–$CsPbI_2Br$ (*hot air method*) and α-$MAPbI_3$ perovskite thin films (*thermal evaporation method*). **d,** structural properties of γ–$CsPbI_2Br$/α-$MAPbI_3$–based H-PHS thin film recorded at a different incident angle (Ω).

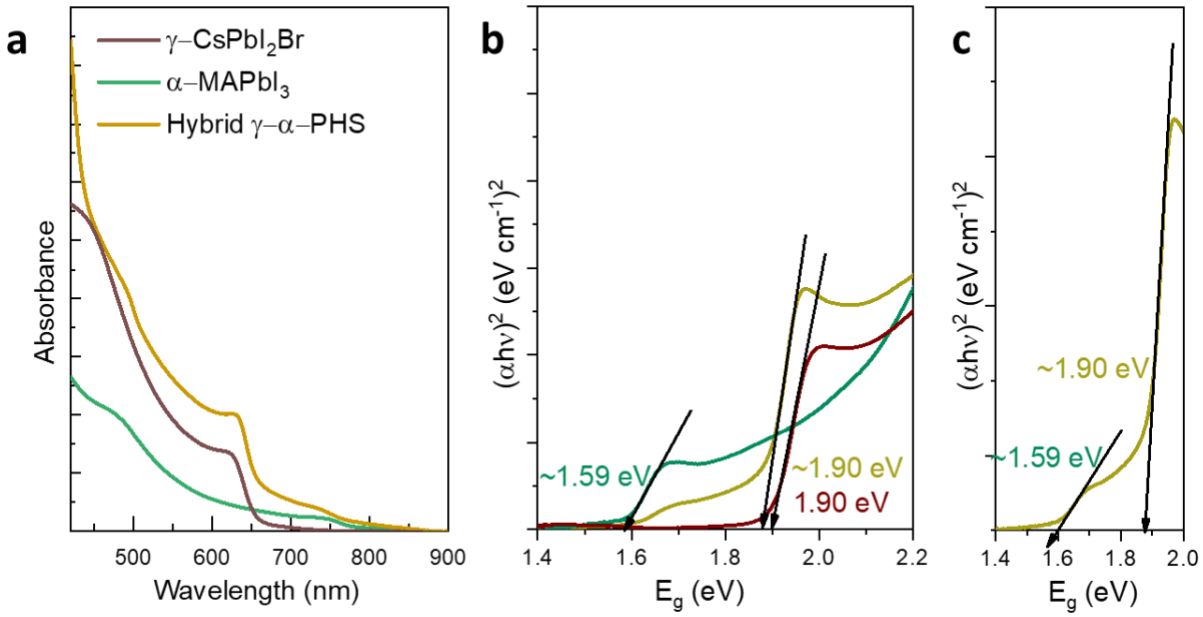

Supplementary Figure 35| Optical properties of the γ–$CsPbI_2Br$/α-$MAPbI_3$-based H-PHS thin films. **a.** UV-Vis optical absorption of γ–$CsPbI_2Br$, α-$MAPbI_3$ and H-PHS thin films. **b**. Tauc plots for respective samples. **c**. Tauc plot of H-PHS showing two independent phases in single H-PHS thin film. The fitting lines in b-c are obtained by a linear fitting of data points.

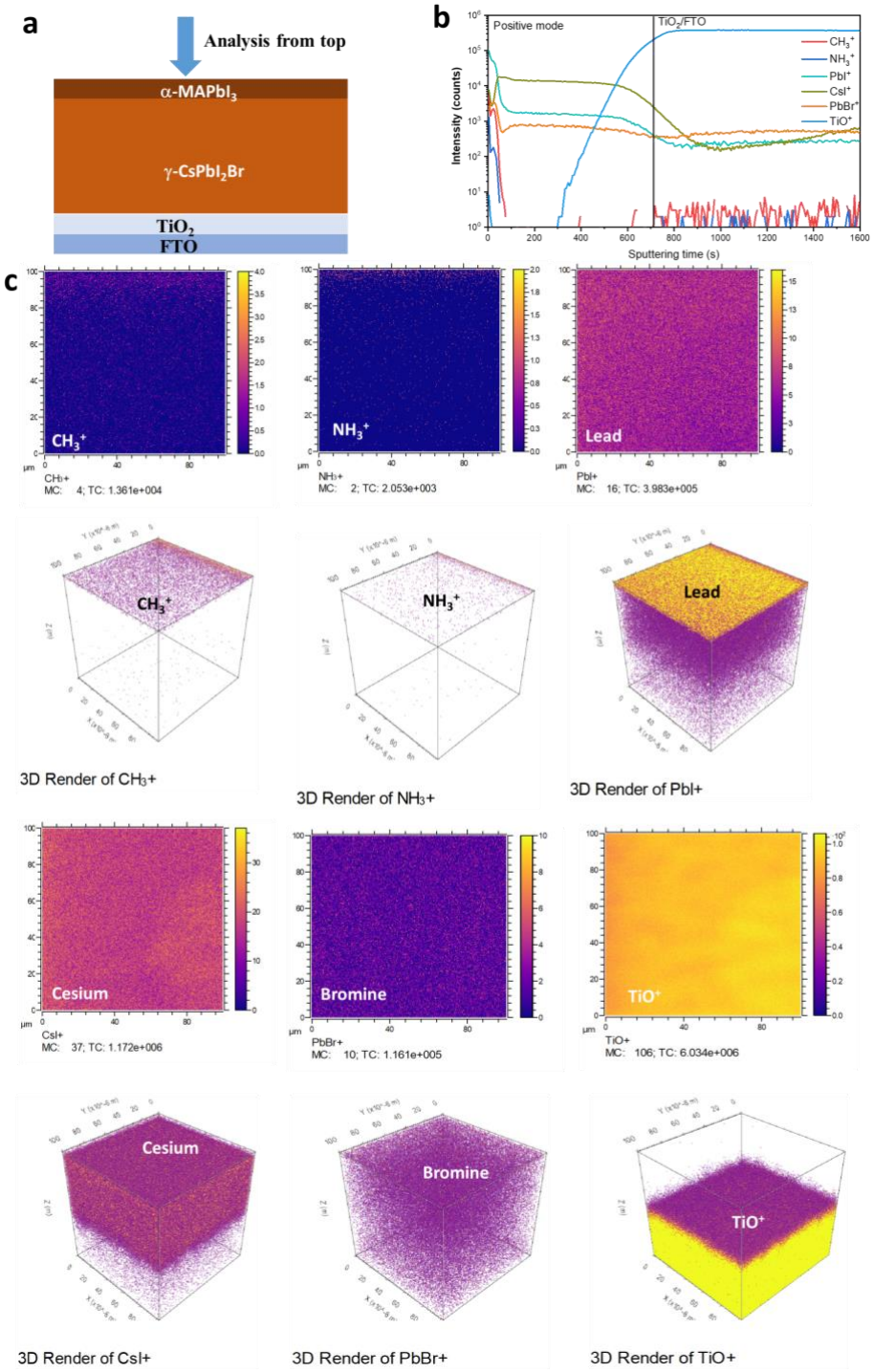

Supplementary Figure 36| a. **ToF:SIMS elemental depth profiles of H-PHS thin film in positive mode**. **a.** Schematic representation of experimental measurements. **b**. Depth-profile analysis TOF-SIMS elemental depth profiles of α-$MAPbI_3$/γ-$CsPbI_2Br$ thin film having FTO/c-TiO_2/perovskite configuration in positive mode. **c.** 2D and 3D renders images for each element.

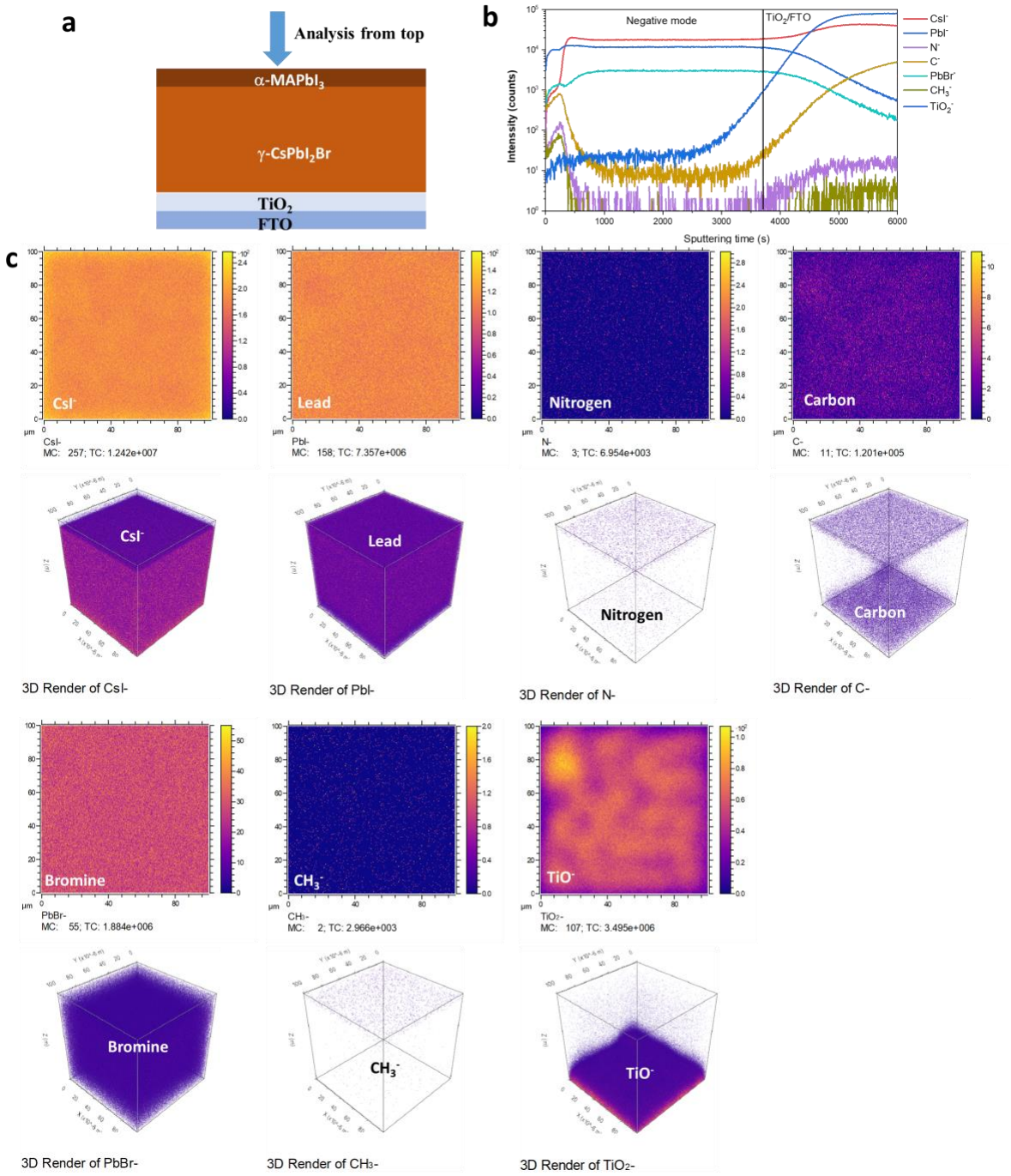

Supplementary Figure 37| a. **ToF:SIMS elemental depth profiles of H-PHS thin film in negative mode**. **a.** Schematic representation of experimental measurements. **b.** Depth-profile analysis TOF-SIMS elemental depth profiles of α-$MAPbI_3$/γ-$CsPbI_2Br$ thin film having FTO/c-TiO_2/perovskite configuration in negative mode. **c.** 2D and 3D renders images for each element.

Supplementary Note 5.

Surface morphology of α-$Cs_{0.05}FA_{0.95}PbI_3$ perovskite thin film

To reveal the surface morphology of bare α-$Cs_{0.05}FA_{0.95}PbI_3$ perovskite film we obtained toop-view SEM as shown in **supplementary Figure 31a**. Top-view SEM image reveals the formation of well-defined grain having 500-600 nm grain size. Interestingly, the cross-sectional SEM image shows the very compact nature of thermally evaporated α-$Cs_{0.05}FA_{0.95}PbI_3$ perovskite thin film with reduced grain boundaries. The XRD analysis clearly reveals the formation pure α-$Cs_{0.05}FA_{0.95}PbI_3$ phase. Our UV-Vis optical absorption analysis clearly revealed that the fabricated α-$Cs_{0.05}FA_{0.95}PbI_3$ perovskite thin films show an absorption band edge at ~820 nm which results in a 1.51 eV band gap. With these optimized conditions, we deposited the α–$Cs_{0.05}FA_{0.95}PbI_3$ perovskite layer onto the γ-$CsPbI_2Br$ film. The resulting α-$Cs_{0.05}FA_{0.95}PbI_3$ film deposited on γ-$CsPbI_2Br$ shows an extra-large grain size of >2 μm compared with that deposited on the c-TiO_2/SnO_2 layer. The cross-sectional SEM image shows a clear formation of two different layers having smooth interface **supplementary Figure 32**.

GIXRD of α-$Cs_{0.05}FA_{0.95}PbI_3$-based H-PHS

To further confirm the structure of the γ-$CsPbI_2Br$/α-$Cs_{0.05}FA_{0.95}PbI_3$ H-PHS, grazing-incidence XRD experiments were performed on the PHJ100 sample by varying the incidence angle Ω from 0.4° to 5° (**Supplementary Figure 32d**). The lower incidence angles are more surface sensitive to rear α-$Cs_{0.05}FA_{0.95}PbI_3$ phase while higher incident angle can detect front absorber. Therefore, we obtained the XRD patterns (measured around ~27 to 31°) show a stronger contribution of α-$Cs_{0.05}FA_{0.95}PbI_3$ (004) diffraction peak, with a smaller contribution of the γ-$CsPbI_2Br$ (200) peak. Increasing Ω from 0.4° to 5° makes the measurement more bulk sensitive, leading to a far stronger signal from the γ-$CsPbI_3$ (200) peak. These measurements confirm the formation of a γ-$CsPbI_2Br$/α-$Cs_{0.05}FA_{0.95}PbI_3$ H-PHS that retains the phase of each of the junction layers. Furthermore, our UV-Vis optical absorption study clearly revealed that presence of two independent phases in the same sample, **Supplementary Figure 33**. Similar results have been observed for *α-$MAPbI_3$-based H-PHS* thin films, **Supplementary Figure 34, 35.**

ToF-SIMS of α-$MAPbI_3$-based H-PHS

The elemental distribution as a function of depth in the γ-$CsPbI_2Br$/α-$MAPbI_3$ (H-PHS) film was measured by TOF-SIMS in positive and negative modes as shown in **Supplementary Figures 36, 37**. Only CH^{3+}, NH^+ along with PbI^+ elements were observed on the surface, which clearly indicates the presence of $MAPbI_3$. However, after 100 sec sputtering time sample exhibited a homogenous distribution of CsI^+, PbI^+ and $PbBr^+$ starts appearing clearly showing the presence of γ-$CsPbI_2Br$ composition when measured in a positive mode. The titanium signal appears after a certain sputtering time (650 sec) and then saturates, indicating the presence of a compact capping layer in the device. In order to track the presence of nitrogen, carbon and CH^{3+} elements more precisely, the TOF-SIMS analysis also in negative mode has been obtained, **Supplementary Figures 37**. Detailed elemental distribution revealed that the carbon and CH^{3+} elements are present only at the surface, while cesium starts appearing after 450 sec. The other elements such as lead, iodine, and bromine were distributed homogeneously up to 3600 sec.

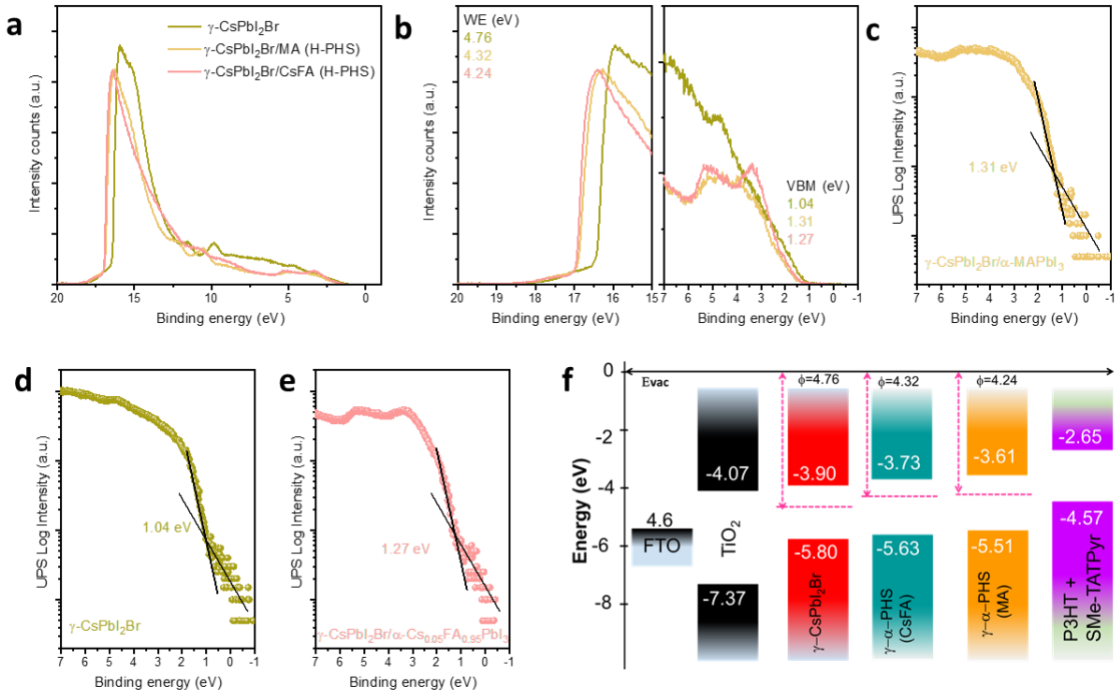

Supplementary Figure 38| γ–$CsPbI_2Br$, γ–$CsPbI_2Br$/α–$Cs_{0.95}FA_{0.95}PbI_3$ (H-PHS), and γ–$CsPbI_2Br$/α–$MAPbI_3$ (H-PHS) interface analysis. **a-e**. Ultraviolet photoelectron spectroscopy (UPS) spectra (using the He−I line with a photon energy of 21.22 eV) corresponding to the secondary electron onset region (WF, work function) and valence band region (VBM, valence band minimum) of the device containing layers with respect to the Fermi energy (w.r.t. E_F). VBM onsets for perovskites were determined from semilog plots. **f**. Energy band levels of the device containing layers. The fitting lines (VBM values) in c-e are obtained by fitting plots guides to the eye.

Supplementary Table 19. Calculated parameters for energy level γ–$CsPbI_2Br$, γ–$CsPbI_2Br$/α–$Cs_{0.95}FA_{0.95}PbI_3$, and γ–$CsPbI_2Br$/α–$MAPbI_3$-based H-PHS devices from UPS analysis.

Sample	**E_{cutoff} (eV) (±0.05)**	**WF (ϕ) (eV)**	**VBM-E_F (eV) (±0.05)**	**VBM (eV)**	**ΔE_g (eV)**	**CBM (eV)**
γ-$CsPbI_2Br$	16.46	4.76	1.04	5.80	1.90	3.90
γ-$CsPbI_2Br$/α-$Cs_{0.05}FA_{0.95}PbI_3$	16.90	4.32	1.31	5.63	1.90	3.73
γ-$CsPbI_2Br$/α-$MAPbI_3$	16.98	4.24	1.27	5.51	1.90	3.61
P3HT+SMe-TATPyr	17.33	3.89	0.68	4.57	1.92	2.65

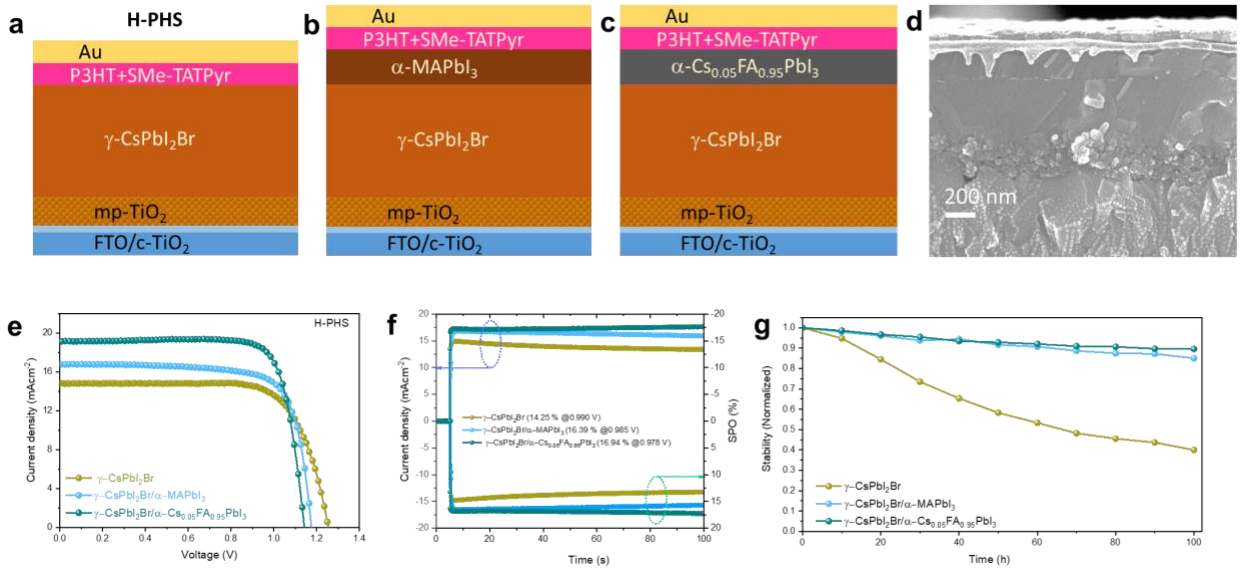

Supplementary Figure 39| a-c. device configuration of H-PHS based on different top-layer. d. cross-sectional SEM image of γ–$CsPbI_2Br$/α-$Cs_{0.05}FA_{0.95}PbI_3$-based H-PHS. **e** Photovoltaics analysis of γ–$CsPbI_2Br$, γ–$CsPbI_2Br$/α-$MAPbI_3$ and γ–$CsPbI_2Br$/α-$Cs_{0.05}FA_{0.95}PbI_3$-based H-PHS devices. **f.** Steady-state current measurements. **g.** Stability of non-encapsulated H-PHS in ambient conditions. Relative humidity 25-30 %. The γ-$CsPbI_2Br$, γ–$CsPbI_2Br$/α-$MAPbI_3$ and γ–$CsPbI_2Br$/α-$Cs_{0.05}FA_{0.95}PbI_3$-based H-PHS devices had initial PCEs of 14.59 %, 15.32, and 17.58 %, respectively.

Supplementary Note 6

Fabrication of hybrid phase heterojunction solar cells (H-PHS)

The γ-$CsPbI_2Br$ front absorber was deposited by the hot-air method as per our previous report. [45] Then annealed γ-$CsPbI_2Br$ thin film was transferred in the vacuum chamber for α-$MAPbI_3$ or α-$Cs_{0.05}FA_{0.95}PbI_3$ perovskite thin films deposition. For α-$MAPbI_3$ two quartz crucibles while three quartz crucibles are used for α-$Cs_{0.05}FA_{0.95}PbI_3$ deposition. Experimental conditions for each layer are summarized in **Supplementary Table 17 and 18.** Quartz crystal microbalances are placed close to the substrate to monitor the evaporation rate. After desired film thickness, samples were vacuum annealed in the thermal evaporator chamber using a substrate heater at 100 and 110 °C respectively for α-$MAPbI_3$ and α-$Cs_{0.05}FA_{0.95}PbI_3$ perovskite thin films and removed from the chamber. The hole-transport layer is deposited on top of the H-PHS thin

films as mentioned before. Finally, 80 nm gold contact was deposited in another thermal evaporation.

Supplementary Figure 39 shows a schematic representation of the H-PHS devices with α-$MAPbI_3$ and α-$Cs_{0.05}FA_{0.95}PbI_3$ rear absorber and γ-$CsPbI_2Br$ front absorber. Representative J-V curves show our γ-$CsPbI_2Br$/α-$MAPbI_3$-based device exhibited a V_{OC} of 1.175 V, a J_{SC} of 16.75 mA cm^{-2}, and a FF of 78.1 %, yielding 15.36 % PCE. In addition, the champion device based on γ-$CsPbI_2Br$/α-$Cs_{0.05}FA_{0.95}PbI_3$ configuration showed an excellent FF of 80%, with a J_{SC} of 19.20 mA cm^{-2}, and a V_{OC} of 1.147 V, yielding efficiency of 17.62 %, **(Supplementary Table 20)**. Detailed SPO and long-term stability analysis revealed clear improvement after α-phase rear absorber deposition.

Although our devices exhibited long-term stability at room temperature, the bilayer or phase-heterojunction stability at higher thermal stress as per International Summit on Organic Photovoltaic Stability (ISOS) protocols (for example T_{65}, T_{85}, T_{100} for 1000 hours) need to be confirm. There might be an ion migration specifically MA^+ /FA^+ cations from rear absorber and reaction between Cs^+ which is reported previously between MA^+ and FA^+ cations. [42] We observed this kind of ion-migration in our H-PHS system which results in alternative third composition once we annealed at higher temperature (170 °C) (*Data not shown in this manuscript*). This is the current limitation of phase heterojunction or bilayer PSC concept for alternative compositions. This ion migration issue may be tackled by inserting oxide tunneling layer (like few nanometers of atomic layer deposited Al_2O_3, ZrO_2, etc. tunneling layers). In addition to ion migration, currently we have only limited perovskite polymorphs like α-$CsPbI_3$, β-$CsPbI_3$ and γ-$CsPbI_3$ while organic-inorganic hybrid perovskites we need to focus of lattice contraction and relaxation or distorted perovskite phases [46] or various compositions and phases of identical perovskite compositions [47] in order to achieve various polymers of hybrid perovskites-based [48] phase-heterojunction solar cell concept.

Supplementary Table 20. Summary of solar cell parameters fabricated based on different thicknesses of rear γ–$CsPbI_3$ perovskites.

Front absorber Hot air	**Rear absorber (thermal Evaporation)**	**V_{OC} (V)**	**J_{SC} ($mAcm^{-2}$)**	**FF (%)**	**PCE (%)**
γ–$CsPbI_2Br$	absent	1.255	14.83	78.5	14.62
	α–$MAPbI_3$	1.175	16.75	78.1	15.36
	α–$Cs_{0.05}FA_{0.95}PbI_3$	1.147	19.20	80.0	17.62

Supplementary Note 7.

The PHS-based perovskite solar mini-module (PSM) consisted of six perovskite subcells connected in series on a 5.22 cm × 5.22 cm substrate with a total active area of 19.17 cm^2. The laser scribing lines P1 and P2 were made by using a CO_2 laser source with 30 and 20 % power respectively. The c-TiO_2/SnO_2 ETL, β–$CsPbI_3$/γ–$CsPbI_3$, and P3HT+Sme-TATPyr HTL layers were prepared following the identical procedure mentioned above for the small-size PSCs. Next line (P2) was conducted using controlled laser power (~6 %) in order to expose the bottom FTO/c-TiO_2/SnO_2 ETL to form the series of connections between cells. A gold top contact with a thickness of 100 nm was then deposited by thermal evaporation. Finally, P3 lines were made by mechanical scribing to separate each subcells. The active area of the perovskite solar modules is (19.17 cm^2) determined by the overlapping regions of the FTO substrate and the Au electrodes. While the exact exposure area excluding the dead area was 18.07 cm^2. Therefore, the geometrical fill factor (GFF) of the mini-module is ~94.2 %.

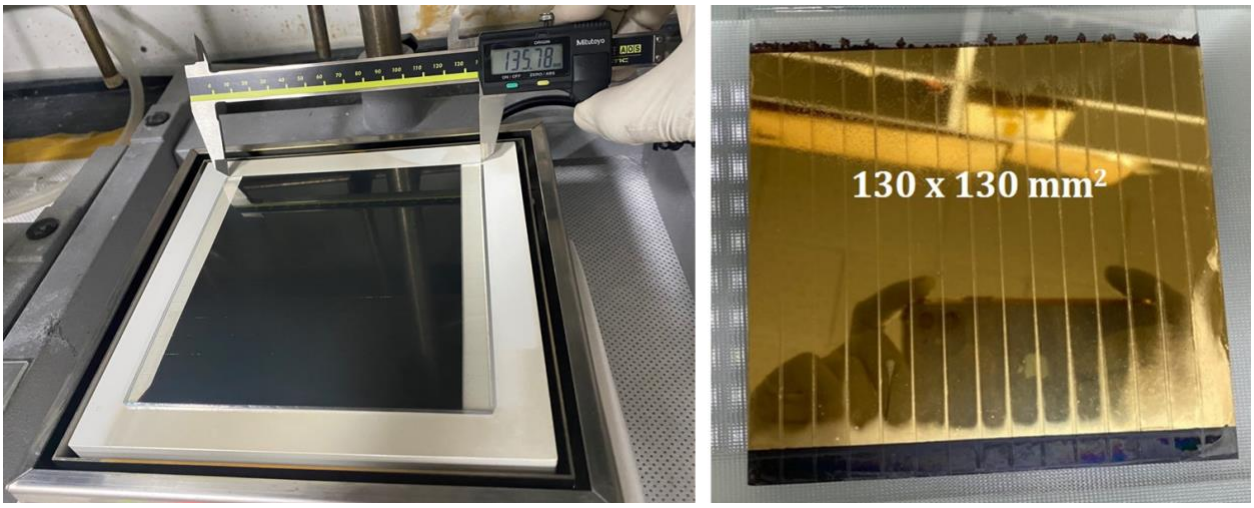

Supplementary Figure 40| Photographs of $CsPbI_3$-based PHS device fabricated by a combination of hot-air assisted blade coating and thermal evaporation method. Left photograph shows ambient stability after γ–$CsPbI_3$-GAI deposition. Right photograph shows the complete PHS module. Both photo credit: Dr. Sawanta S. Mali

Supplementary Note 8.

In order to make an ultra-large (130 × 130 mm^2) PHS module, c-TiO_2 and SnO_2 bilayer ETL was obtained by an indigenous spray coating method. The ETL precursors were prepared as follows; for c-TiO_2 spray solution, 50 mL ethanol solution containing 3 mL titanium diisopropoxide bis(acetylacetonate) and 2 mL acetylacetone at 350 °C. After deposition samples were further annealed in a muffle furnace for the next 30 min at 450 °C. The SnO_2 solution was prepared as the same recipe discussed above and sprayed 30 mL at 180 °C. For the front β–$CsPbI_3$ absorber layer was achieved by the hot-air assisted blade coating method followed by annealing at 210 °C for 20 min. For γ–$CsPbI_3$-GAI deposition we followed the same deposition method as discussed above, (**Supplementary Movies 1, 2**). The P3HT+SME-TAPyr HTL was blade coated in ambient conditions and then annealed. The P1 and P2 laser scribing is done by the above protocol. Top gold contact (120 nm) was made by the thermal evaporation method.

References

[1] Oliver, R. D. J. et al. Thermally Stable Passivation Toward High Efficiency Inverted Perovskite Solar Cells. *ACS Energy Lett*. **5**, 3336−3343 (2020). https://doi.org/10.1021/acsenergylett.0c01813

[2] Stolterfoht, M., Caprioglio, P., Wolff, C. M., Marquez, J. A., Nordmann, J., Zhang, S., Rothhardt, D., Hormann, U., Amir, Y., Redinger, A., Kegelmann, L., Zu, F., Albrecht, S., Koch, N., Kirchartz, T., Saliba, M., Unold, T. & Neher, D. The Impact of Energy Alignment and Interfacial Recombination on the Internal and External Open-Circuit Voltage of Perovskite Solar Cells. *Energy Environ. Sci.* **12**, 2778–2788 (2019). https://doi.org/10.1039/C9EE02020A

[3] Lakowicz, J. R. Principles of Fluorescence Spectroscopy. *Springer*, (2006) https://link.springer.com/book/10.1007/978-0-387-46312-4

[4] Sillen, A. & Engenborghs, Y. The Correct Use of "Average" Fluorescence Parameters, *Photochem. Photobiol.* **67**, 475-486 (1998). https://doi.org/10.1111/j.17511097.1998.tb09082.x

[5] Eperon, G. E., Paternò, G. M., Sutton, R. J., Zampetti, A., Haghighirad, A. A., Cacialli, F. & Snaith, H. J. Inorganic caesium lead iodide perovskite solar cells. *J. Mater. Chem. A* **3**, 19688-19695 (2015). https://doi.org/10.1039/C5TA06398A

[6] Swarnkar, A. *et al.* Quantum dot–induced phase stabilization of α-$CsPbI_3$ perovskite for high-efficiency photovoltaics. *Science* **354**, 92-95 (2016). https://doi.org/10.1126/science.aag2700

[7] Wang, Q. *et al.* Stabilizing the α-Phase of $CsPbI_3$ Perovskite by Sulfobetaine Zwitterions in One-Step Spin-Coating Films. *Joule* **1**, 371-382 (2017). https://doi.org/10.1016/j.joule.2017.07.017

[8] Zhang, T. *et al.* Bication lead iodide 2D perovskite component to stabilize inorganic α-$CsPbI_3$ perovskite phase for high-efficiency solar cells. *Sci. Adv.* **3,** e1700841 (2017). https://doi.org/10.1126/sciadv.1700841

[9] Sanehira, E. M. *et al.* Enhanced mobility $CsPbI_3$ quantum dot arrays for record-efficiency, high-voltage photovoltaic cells. *Sci. Adv.* **3,** eaao4204 (2017). https://doi.org/10.1126/sciadv.aao4204

[10] Wang, Y. *et al.* Bifunctional Stabilization of All-Inorganic α-$CsPbI_3$ Perovskite for 17% Efficiency Photovoltaics. *J. Am. Chem. Soc.* **140**, 39, 12345–12348 (2018). https://doi.org/10.1021/jacs.8b07927

[11] Chen, K. *et al.* High Efficiency Mesoscopic Solar Cells Using $CsPbI_3$ Perovskite Quantum Dots Enabled by Chemical Interface Engineering. *J. Am. Chem. Soc.* **142,** 3775–3783(2020). https://doi.org/10.1021/jacs.9b10700

[12] Chen, R. *et al.* Moisture-tolerant and high-quality α-$CsPbI_3$ films for efficient and stable perovskite solar modules. *J. Mater. Chem. A* **8**, 9597-9606 (2020). https://doi.org/10.1039/D0TA01968B

[13] Jia, D. *et al.* Tailoring solvent-mediated ligand exchange for $CsPbI_3$ perovskite quantum dot solar cells with efficiency exceeding 16.5%. *Joule* **6**, 632-1653 (2022). https://doi.org/10.1016/j.joule.2022.05.007

[14] Wu, T. *et al.* Efficient and Stable $CsPbI_3$ Solar Cells via Regulating Lattice Distortion with Surface Organic Terminal Groups. *Adv. Mater.* **31**, 1900605 (2019). https://doi.org/10.1002/adma.201900605

[15] Wang, J. *et al.* Highly efficient all-inorganic perovskite solar cells with suppressed non-radiative recombination by a Lewis base. *Nat. Commun.* **11**, 177 (2020). https://doi.org/10.1038/s41467-019-13909-5

[16] Chang, X. *et al.* Printable $CsPbI_3$ Perovskite Solar Cells with PCE of 19% via an Additive Strategy. *Adv. Mater.* **32**, 2001243 (2020). https://doi.org/10.1002/adma.202001243

[17] Fu, S. *et al.* Humidity-Assisted Chlorination with Solid Protection Strategy for Efficient Air-Fabricated Inverted $CsPbI_3$ Perovskite Solar Cells. *ACS Energy Lett.* **6**, 10, 3661–3668 (2021). https://doi.org/10.1021/acsenergylett.1c01817

[18] Ran, J. *et al.* Perovskite phase heterojunction solar cells. *Nat. Energy* **7**, 1170-1179 (2022). https://doi.org/10.1038/s41560-022-01154-y

[19] This work (for β–$CsPbI_3$-based p-i-n configuration).

[20] Wang, Y. *et al.* Thermodynamically stabilized β-$CsPbI_3$–based perovskite solar cells with efficiencies >18%. *Science*, **365,** 591-595 (2019). https://doi.org/10.1126/science.aav8680

[21] Ye, Q. *et al.* Cesium Lead Inorganic Solar Cell with Efficiency beyond 18% via Reduced Charge Recombination. *Adv. Mater.* **31**, 1905143 (2019). https://doi.org/10.1002/adma.201905143

[22] Wang, Y. *et al.* The Role of Dimethylammonium Iodide in $CsPbI_3$ Perovskite Fabrication: Additive or Dopant? *Angew. Chem. Int. Ed*. **58**, 16691-16696 (2019). https://doi.org/10.1002/ange.201910800

[23] Fu, S. *et al.* Tailoring In Situ Healing and Stabilizing Post-Treatment Agent for High-Performance Inverted $CsPbI_3$ Perovskite Solar Cells with Efficiency of 16.67%. *ACS Energy Lett.* **5,** 3314-3321 (2020). https://doi.org/10.1021/acsenergylett.0c01728

[24] Wang, Y. *et al.* High Phase Stability in $CsPbI_3$ Enabled by Pb–I Octahedra Anchors for Efficient Inorganic Perovskite Photovoltaics. *Adv. Mater.* **32**, 2000186 (2020). https://doi.org/10.1002/adma.202000186

[25] Wang, K. *et al.* In-Situ Hot Oxygen Cleansing and Passivation for All-Inorganic Perovskite Solar Cells Deposited in Ambient to Breakthrough 19% Efficiency. *Adv. Funct. Mater.* **31**, 2101568 (2021). https://doi.org/10.1002/adfm.202101568

[26] Yu, B. *et al.* Efficient (>20 %) and Stable All-Inorganic Cesium Lead Triiodide Solar Cell Enabled by Thiocyanate Molten Salts. *Angew. Chem. Int. Ed.* **60,** 13436-13443 (2021). https://doi.org/10.1002/anie.202102466

[27] Yoon, S. M. *et al.* Surface Engineering of Ambient-Air-Processed Cesium Lead Triiodide Layers for Efficient Solar Cells. *Joule* **5**, 183-196 (2021). https://doi.org/10.1016/j.joule.2020.11.020

[28] Wang, X. *et al.* Efficient and Stable $CsPbI_3$ Inorganic Perovskite Photovoltaics Enabled by Crystal Secondary Growth. *Adv. Mater.* **33**, 2103688 (2021). https://doi.org/10.1002/adma.202103688

[29] Sun, X. *et al.* Highly efficient $CsPbI_3/Cs_{1-x}DMA_xPbI_3$ bulk heterojunction perovskite solar cell. *Joule* **6**, 850-860 (2022). https://doi.org/10.1016/j.joule.2022.02.004

[30] This work (for β–$CsPbI_3$-based n-i-p configuration).

[31] Monroy, M. I. P. *et al.* All-Evaporated, All-Inorganic $CsPbI_3$ Perovskite-Based Devices for Broad-Band Photodetector and Solar Cell Applications. *ACS Appl. Electron. Mater*. **3**, 3023–3033 (2021) https://doi.org/10.1021/acsaelm.1c00252 .

[32] Zhang, Z. *et al.* Efficient Thermally Evaporated γ-$CsPbI_3$ Perovskite Solar Cells. *Adv. Energy Mater.* **11**, 2100299 (2021). https://doi.org/10.1002/aenm.202100299

[33] Lu, C. *et al.* Efficient inverted $CsPbI_3$ perovskite solar cells fabricated in common air. *Chem. Eng. J.* **452**, 139495(2023). https://doi.org/10.1016/j.cej.2022.139495

[34] Choi, H. et al. Cesium-doped methylammonium lead iodide perovskite light absorber for hybrid solar cells. *Nano Energy*, **7**, 80-85 (2014). https://doi.org/10.1016/j.nanoen.2014.04.017

[35] *Zhao, B. et al.* Thermodynamically Stable Orthorhombic γ-$CsPbI_3$ Thin Films for High-Performance Photovoltaics. *J. Am. Chem. Soc.* **140**, 11716–11725 (2018). https://doi.org/10.1021/jacs.8b06050

[36] Wang, K. *et al.* All-inorganic cesium lead iodide perovskite solar cells with stabilized efficiency beyond 15%. *Nat. Commun.* **9**, 4544 (2018). https://doi.org/10.1038/s41467-018-06915-6

[37] Gu, X. *et al.* Rational Surface-Defect Control via Designed Passivation for High-Efficiency Inorganic Perovskite Solar Cells. *Angew. Chem.* **133**, 23348 –23354 (2021). https://doi.org/10.1002/ange.202109724

[38] Duan, L. *et al.* Phase-Pure γ-$CsPbI_3$ for Efficient Inorganic Perovskite Solar Cells. *ACS Energy Lett.* 7, 2911–2918 (2022). https://doi.org/10.1021/acsenergylett.2c01219

[39] Tan, S. *et al.* Temperature-Reliable Low-Dimensional Perovskites Passivated Black-Phase $CsPbI_3$ toward Stable and Efficient Photovoltaics. *Angew. Chem. Int. Ed.* **61**, e202201300 (2022). https://doi.org/10.1002/anie.202201300

[40] Wang, J. *et al.* 21.15%-Efficiency and Stable γ-$CsPbI_3$ Perovskite Solar Cells Enabled by an Acyloin Ligand. *Adv. Mater.* **35**, 2210223 (2023). https://doi.org/10.1002/adma.202210223

[41] Clifford, J. P., Johnston, K. W., Levina, L. & Sargent, E. H. Schottky barriers to colloidal quantum dot films. *Appl. Phys. Lett.* **91**, 253117 (2007). https://doi.org/10.1063/1.2823582

[42] Clark, C. P., Mann, J. E., Bangsund, J. S., Hsu, W.-J., Aydil, E. S. & Holmes, R. J. Formation of Stable Metal Halide Perovskite/Perovskite Heterojunctions *ACS Energy Lett.* **5**, 3443-3451 (2020). https://doi.org/10.1021/acsenergylett.0c01609

[43] Li, F., Zhou, S., Yuan, J., Qin, C., Yang, Y., Shi, J., Ling, X., Li, Y. & Ma, W. Perovskite Quantum Dot Solar Cells with 15.6% Efficiency and Improved Stability Enabled by an α-$CsPbI_3$/$FAPbI_3$ Bilayer Structure *ACS Energy Lett.* **4**, 2571−2578 (2019). https://doi.org/10.1021/acsenergylett.9b01920

[44] Sidhik, S., Wang, Y., De Siena, M., Asadpour, R., Torma, A. J., Terlier, T., Ho, K., Li, W., Puthirath, A. B., Shuai, X., Agrawal, A., Traore, B., Jones, M., Giridharagopal, R., Ajayan, P. M., Strzalka, J., Ginger, D. S., Katan, C., Alam, M. A., Even, J., Kanatzidis, M. G. & Mohite, A. D. Deterministic fabrication of 3D/2D perovskite bilayer stacks for durable and efficient solar cells. *Science* **377**, 1425-1430 (2022). https://doi.org/10.1126/science.abq7652

[45] Mali, S. S., Patil, J. V., Shinde, P. S., Miguel, G. & Hong, C. K. Fully Air-Processed Dynamic Hot-Air-Assisted M:$CsPbI_2Br$ (M: Eu^{2+}, In^{3+}) for Stable Inorganic Perovskite Solar Cells. *Matter* **4**, 635-653 (2021). https://doi.org/10.1016/j.matt.2020.11.008.

[46] Prasanna, R., Gold-Parker, A., Leijtens, T., Conings, B., Babayigit, A., Boyen, H.-G., Toney, M. F. & McGehee, M. D. Band Gap Tuning via Lattice Contraction and Octahedral Tilting in Perovskite Materials for Photovoltaics. *J. Am. Chem. Soc.* **139**, 32, 11117–11124 (2017). https://doi.org/10.1021/jacs.7b04981

[47] Tao, S., Schmidt, I., Brocks, G., Jiang, J., Tranca, I., Meerholz, K. & Olthof, S. Absolute energy level positions in tin- and lead-based halide perovskites. *Nat. Commun.* **10**, 2560 (2019). https://doi.org/10.1038/s41467-019-10468-7

[48] Oku, T. Crystal structures of perovskite halide compounds used for solar cells. *Rev. Adv. Mater. Sci.* **59**, 264–305 (2020). https://doi.org/10.1515/rams-2020-0015